

Fundamental Limits in Multi-image Alignment

Cecilia Aguerrebere, Mauricio Delbracio, Alberto Bartesaghi and Guillermo Sapiro

Abstract—The performance of multi-image alignment, bringing different images into one coordinate system, is critical in many applications with varied signal-to-noise ratio (SNR) conditions. A great amount of effort is being invested into developing methods to solve this problem. Several important questions thus arise, including: Which are the fundamental limits in multi-image alignment performance? Does having access to more images improve the alignment? Theoretical bounds provide a fundamental benchmark to compare methods and can help establish whether improvements can be made. In this work, we tackle the problem of finding the performance limits in image registration when multiple shifted and noisy observations are available. We derive and analyze the Cramér-Rao and Ziv-Zakai lower bounds under different statistical models for the underlying image. The accuracy of the derived bounds is experimentally assessed through a comparison to the maximum likelihood estimator. We show the existence of different behavior zones depending on the difficulty level of the problem, given by the SNR conditions of the input images. We find that increasing the number of images is only useful below a certain SNR threshold, above which the pairwise MLE estimation proves to be optimal. The analysis we present here brings further insight into the fundamental limitations of the multi-image alignment problem.

Index Terms—Multi-image alignment, performance bounds, Cramér-Rao bound, Ziv-Zakai bound, Bayesian Cramér-Rao, maximum likelihood estimator.

I. INTRODUCTION

Multi-image alignment consists in registering a group of images to a common reference.¹ The multi-image alignment problem is ubiquitous in many fundamental image processing applications such as high dynamic range imaging [1], [2], super resolution [3], [4], [5], burst denoising [6] and burst deblurring [7], [8]. Indeed, this problem is of great importance for very different domains, such as biomedical imaging, astronomy and remote sensing, where due to physical or biological constraints the photographing system captures a series of unregistered and often noisy images.

Various methods have been proposed for multi-image alignment [9], [10], [11], [12], [13], [4] and a great amount of effort is being invested to further improve their performance, mostly in applications that deal with very low signal-to-noise ratio (SNR) conditions [14], [15], [16], [17]. Hence, an important question arises: Which are the fundamental limits on multi-image alignment performance? Theoretical performance bounds provide a fundamental benchmark to compare different

methods and can help establish whether improvements can be made. In this work, we tackle the problem of finding the performance limits in image registration when multiple shifted and noisy observations are available.

Theoretical statistical performance bounds are of great interest and have been used in a wide variety of signal processing problems. One of the most widely used approaches, probably because of its simplicity, is the Cramér-Rao bound (CRB) [18], which establishes a lower bound on the variance of any unbiased estimator of the parameter of interest. For instance, CRBs have been previously used to establish performance limits in pairwise image alignment [19], [20], super-resolution [3], high dynamic range imaging [21] and image denoising [22], among others. Another example is the bound proposed by Ziv and Zakai [23] and its extensions [24], [25], [26]. They proposed to relate the mean squared error of the estimator to the probability of error in a binary detection problem, leading in general to tighter bounds than the CRB. Examples of the application of the Ziv-Zakai bound (ZZB) to practical problems can be found in pairwise image alignment [27] and time delay estimation [28], [29], among others. Both the CRB and the ZZB will be computed here for the problem of multi-image alignment.

Image registration can easily become very complex with the kind of scene motions we face in real world scenarios. In this work, we focus on global translation which, despite being the most basic motion model, is of great interest because it is present in almost all applications. The considered motion model is thus given by

$$z(\mathbf{x}) = u(\mathbf{x} - \boldsymbol{\tau}) + n(\mathbf{x}), \quad (1)$$

where $z(\mathbf{x})$ is the observed image at pixel position \mathbf{x} , u is the underlying image, $\boldsymbol{\tau}$ is the 2D translation vector and $n(\mathbf{x})$ is additive white Gaussian noise independent of u .

A fundamental aspect that has to be considered when computing a performance bound for the image alignment problem under Model (1), is how to characterize the underlying image u . Even if the parameter of interest is the shift vector $\boldsymbol{\tau}$, assumptions have to be made about u and each assumption will lead to different performance bounds. For instance, u could be considered as deterministic, known or unknown, or as a realization of a known random process.

Various performance bounds have been derived for the pairwise image alignment problem (i.e., registration between two images) assuming a deterministic *known* underlying image. Examples of this are the CRB for translation estimation derived by Robinson and Milanfar [19], the CRB for general parametric registration introduced by Pham *et al.* [20], and the ZZB derived by Xu *et al.* [27] for rigid pairwise registration including translation and rotation.

C. Aguerrebere, M. Delbracio and G. Sapiro are with the Department of Electrical and Computer Engineering at Duke University. A. Bartesaghi is with the Laboratory of Cell Biology, Center for Cancer Research, National Cancer Institute, National Institutes of Health.
e-mail: {cecilia.aguerrebere, mauricio.delbracio, guillermo.sapiro}@duke.edu, bartesaghi@mail.nih.gov

¹We use hereafter the terms image alignment and image registration interchangeably.

Regarding multi-image alignment, a specific case was analyzed by Rais *et al.* [30], who computed the CRB for the registration of a group of Earth satellite images that were uniformly translated, i.e., all shifts are multiples of a single unknown value that needs to be estimated. In [3], Robinson and Milanfar presented a thorough statistical performance analysis on super-resolution, of which multi-image registration is typically a major component. They studied translation estimation and image reconstruction jointly, thus assuming an *unknown* underlying image. This work shed light on image super-resolution, giving important insight into which are the main bottlenecks for improving performance. They derived bounds for the combined problem under two different assumptions for u : the CRB assuming an unknown deterministic image and a Bayesian CRB assuming a Gaussian prior for u . In both cases, and assuming the considered images are aliasing free, the computed CRB for the multiple shifts estimation was independent of the number of available images.

It is interesting to remark that the problem of image translation estimation is closely related to the problem of time delay estimation of a signal observed at two or more spatially separated receivers [28], [29]. Indeed, our analysis follows and extends the results from [29] to the case where multiple noisy versions of the same flat spectrum signal are observed, each with a different shift.

In this work, we derive and analyze various performance bounds for the multi-image alignment problem under two different models for the underlying image u . First, we consider u to be deterministic and unknown. Under this image model, we compute the CRB and a Bayesian CRB assuming a generalized Gaussian prior for the shifts. Second, assuming a stochastic Gaussian model for the underlying image u , we derive the CRB and the extended Ziv-Zakai bounds (EZZB).

A thorough analysis is conducted, which unveils the similarities between these seemingly different approaches. We find a *per-region* behavior depending on the difficulty level of the problem, given by the SNR conditions. For certain SNR values, performance depends on the number of images. Also, it degrades dramatically below a given threshold, until reaching a region where the SNR is too low to enable alignment.

In order to assess the tightness of the computed bounds, we compare them to the alignment accuracy obtained by the maximum likelihood estimator (MLE). The MLE, besides being a widely used estimator, is known to be asymptotically efficient and also efficient for any number of observations in various problems [21]. A *per-region* behavior depending on the SNR level, similar to the one predicted by the EZZB, is observed for the MLE as well. We find that all the computed bounds are very tight in very high SNR conditions, where the MLE achieves them and is thus efficient. For such high SNR, we find that the alignment performance only depends on the ratio between the energy of the image gradient and the noise level, and does not depend on the number of available images. Hence, for very high SNR, multi-image alignment can be performed in a pairwise fashion without losing information.

However, this is not the case for low SNR where the performance shows a dependence on the number of images, until reaching a steady state error for extremely low SNR where

z_i, u	Images defined in continuous domain $\mathbf{x} = [x, y] \in \mathbb{R}^2$
\mathbf{z}_i, \mathbf{u}	Digital images sampled on discrete grid $m_r \times m_c$
$\mathbf{u}_x, \mathbf{u}_y$	Derivatives of \mathbf{u} in direction x and y
K	Number of unknown translations
$\boldsymbol{\tau}_i$	2D translation vector $\boldsymbol{\tau}_i = [\tau_{i_x}, \tau_{i_y}]^T$ of image i
$\boldsymbol{\tau}$	Concatenation of K 2D translations
\tilde{z}_i, \tilde{u}	Fourier transform of images z_i, u
$\tilde{\mathbf{z}}$	Concatenation of $(K + 1)$ Fourier transforms $\tilde{\mathbf{z}}_i$
$\boldsymbol{\omega}$	2D Fourier spatial frequency $\boldsymbol{\omega} = [\omega_x, \omega_y]^T$
$S(\boldsymbol{\omega})$	Power spectral density of 2D random process \mathbf{u}
$\mathbf{J}_D, \mathbf{J}_S$	Fisher information matrices
MSE	Mean square error
EMSE	Expected mean square error
SNR	Signal-to-noise ratio as defined by Eq. (43)
CRBD	Cramér-Rao bound under deterministic image model Eq. (16)
BCRB	Bayesian Cramér-Rao bound (with shift prior) Eq. (28)
CRBS	Cramér-Rao bound under stochastic image model Eq. (40)
EZZB _w	Extended Ziv-Zakai bound (flat spectrum) Eq. (63)

Table I: Summary of notation used in this article.

alignment is not possible. The SNR values delimiting these regions, which are of particular importance in practice, are also derived and found to depend on the number of available images. Therefore, increasing the number of images is useful since, not only it improves the achievable performance, but it also shifts the SNR thresholds making alignment possible for a larger noise level range.

This article is organized as follows. Section II presents the statistical framework used to state multi-image alignment as a parameter estimation problem. Sections III and IV are devoted to the computation and analysis of the different performance bounds, under the deterministic and stochastic image models respectively. Section V presents an analysis and comparison of all the computed bounds. The bounds accuracy is assessed in Section VI. Section VII summarizes the conclusions.

II. MULTI-IMAGE REGISTRATION: AN ESTIMATION PROBLEM

In what follows, we present the image model used throughout the article for the derivation of the different performance bounds. Also, we introduce the performance indicators used to evaluate the translation estimators. Table I summarizes the notation used in the article.

A. Image model

Let us consider the image acquisition model:

$$z_i(\mathbf{x}) = u(\mathbf{x} - \boldsymbol{\tau}_i) + n_i(\mathbf{x}), \quad i = 0, \dots, K, \quad (2)$$

where $z_i(\mathbf{x})$ is the observed i -th image at pixel position $\mathbf{x} = [x, y]^T \in \mathbb{R}^2$, $u(\mathbf{x})$ is the underlying continuous image generating the noisy shifted observations, $\boldsymbol{\tau}_i = [\tau_{i_x}, \tau_{i_y}]^T \in \mathbb{R}^2$ is the 2D translation vector of frame i with respect to the underlying image u (frame zero, $\boldsymbol{\tau}_0 = 0$), and $n_i(\mathbf{x})$ is additive Gaussian noise assumed to be independent of u .

In practice, we do not have access to the continuous images but to a finite discretization of them. We will assume that all the images are band-limited and sampled according to the Nyquist sampling theorem. Regarding the finite observation support, we will additionally assume that the energy of the

signal outside the observed sampling grid is negligible. These two assumptions guarantee an almost perfect interpolation of the *continuous* images from the *digital* ones. Thus, under this ideal framework, we are able to compute image derivatives or image shifts (or any other linear operator) directly from the discrete samples. Although we will omit the details for simplicity, all the considered operators could be computed via Fourier interpolation (e.g., using the DFT). Let us assume that the digital images are indexed into vectors of size $N_p = m_r \times m_c$ pixels, where m_r and m_c are the number of rows and columns respectively.

Let $\boldsymbol{\tau} = [\boldsymbol{\tau}_1^T, \dots, \boldsymbol{\tau}_K^T]^T \in \mathbb{R}^{2K}$ be the concatenation of all 2D unknown translations, and $\mathbf{z} = [\mathbf{z}_0^T, \dots, \mathbf{z}_K^T]^T \in \mathbb{R}^{(K+1)N_p}$ be the concatenation of the $(K+1)$ observed images. The goal in multi-image alignment is then to estimate $\boldsymbol{\tau}$ from \mathbf{z} .

B. Performance evaluation

Let us call $\boldsymbol{\theta}$ the vector of parameters to be estimated, e.g. $\boldsymbol{\theta} = \boldsymbol{\tau}$. Given any estimate $\hat{\boldsymbol{\theta}}(\mathbf{z})$ of $\boldsymbol{\theta}$, its performance can be measured through the error correlation matrix,

$$\mathbf{R}_\epsilon = \mathbb{E}_{\mathbf{z}|\boldsymbol{\theta}}[\boldsymbol{\epsilon}\boldsymbol{\epsilon}^T], \quad (3)$$

where $\boldsymbol{\epsilon} = \hat{\boldsymbol{\theta}} - \boldsymbol{\theta}$ is the error with respect to the real parameter value and $\mathbb{E}_{\mathbf{z}|\boldsymbol{\theta}}[\cdot]$ is the expected value over the observed data distribution given $\boldsymbol{\theta}$. The fundamental limits on the estimation of $\boldsymbol{\theta}$ can be stated through the family of performance bounds which consider the parameter as an unknown *deterministic* quantity and provide a limit on \mathbf{R}_ϵ . Examples of this family are the Cramér-Rao [18], Bhattacharyya [31], Barankin [32], and Abel [33] bounds, among others.

In some cases, prior information is known about $\boldsymbol{\theta}$. This motivates the development of the *Bayesian* bounds, which model the parameter as a *random variable* with a known *prior* distribution, and give a limit on the expected error correlation matrix under the joint distribution of the data and the parameter

$$\bar{\mathbf{R}}_\epsilon = \mathbb{E}_{\mathbf{z},\boldsymbol{\theta}}[\boldsymbol{\epsilon}\boldsymbol{\epsilon}^T]. \quad (4)$$

Examples of Bayesian bounds are the Bayesian Cramér-Rao [34], the Ziv-Zakai [23], and the Weiss-Weinstein [35] bounds.

A more practical performance indicator is the mean squared error of the estimated parameters, which corresponds to the trace of the error correlation matrix. We refer hereafter as mean squared error (MSE) to the trace of \mathbf{R}_ϵ and expected mean squared error (EMSE) to the trace of $\bar{\mathbf{R}}_\epsilon$.

In the following sections, we compute and analyze variants of two performance bounds for the multi-image alignment problem, the Cramér-Rao [18] and the Extended Ziv-Zakai lower bounds [26]. The performance analysis is conducted under two different hypothesis for the unknown underlying image: \mathbf{u} is a deterministic unknown image (Section III), and \mathbf{u} is a realization of a zero mean Gaussian random process with known covariance matrix (Section IV). Although the Gaussian model is over-simplistic [36], it is nonetheless interesting, not only because of its practicality, but also because it has proven to be very powerful for locally modeling natural images in several applications [37], [38], [39], [40].

III. PERFORMANCE BOUNDS: DETERMINISTIC IMAGE MODEL

In this section, we assume that \mathbf{u} is an unknown deterministic digital image. We also assume that the noise in the digital observations \mathbf{n} has a diagonal covariance matrix $\sigma^2 \mathbf{I}$. Notice that, even if the goal of multi-image registration is to estimate $\boldsymbol{\tau}$ and not \mathbf{u} , the latter is unknown and needs to be accounted for in the analysis. This kind of parameters, whose estimation is not of direct interest but because they are related to the analysis have to be accounted for, are commonly referred to as nuisance parameters [41]. Hence, the parameter vector becomes $\boldsymbol{\theta} = [\mathbf{u}^T, \boldsymbol{\tau}^T]^T$, where we are only interested in estimating $\boldsymbol{\tau}$ from the $(K+1)$ noisy observed images \mathbf{z} .

A. Cramér-Rao lower bound: deterministic image model

The performance of any unbiased estimator $\hat{\boldsymbol{\theta}}(\mathbf{z})$ of $\boldsymbol{\theta}$ is bounded by the CRB [18]

$$\mathbf{R}_\epsilon \geq \mathbf{J}^{-1}, \quad (5)$$

where \mathbf{J} is the Fisher information matrix (FIM) given by

$$\{\mathbf{J}\}_{i,j} = -\mathbb{E}_{\mathbf{z}|\boldsymbol{\theta}} \left[\frac{\partial^2 \ell(\mathbf{z}; \boldsymbol{\theta})}{\partial \theta_i \partial \theta_j} \right], \quad (6)$$

and $\ell(\mathbf{z}; \boldsymbol{\theta}) = \log(p(\mathbf{z}; \boldsymbol{\theta}))$ is the logarithm of the likelihood function. The FIM in this case can be expressed as

$$\mathbf{J}_D = \begin{bmatrix} \mathbf{J}_{\mathbf{u}\mathbf{u}} & \mathbf{J}_{\mathbf{u}\boldsymbol{\tau}}^T \\ \mathbf{J}_{\mathbf{u}\boldsymbol{\tau}} & \mathbf{J}_{\boldsymbol{\tau}\boldsymbol{\tau}} \end{bmatrix}, \quad (7)$$

where the term $\mathbf{J}_{\mathbf{u}\mathbf{u}}$ captures the information provided by the image only, the term $\mathbf{J}_{\boldsymbol{\tau}\boldsymbol{\tau}}$ captures the available information of the translations and $\mathbf{J}_{\mathbf{u}\boldsymbol{\tau}}$ represents the information provided by the intercorrelation between \mathbf{u} and $\boldsymbol{\tau}$. Using the block matrix inversion principle [42], the inverse of \mathbf{J} can be expressed as

$$\mathbf{J}_D^{-1} = \begin{bmatrix} \mathbf{S}_{\mathbf{u}}^{-1} & \mathbf{J}_{\mathbf{u}\boldsymbol{\tau}}^{-1} \mathbf{J}_{\boldsymbol{\tau}\boldsymbol{\tau}}^{-1} \mathbf{S}_{\boldsymbol{\tau}}^{-1} \\ \mathbf{S}_{\boldsymbol{\tau}}^{-1} \mathbf{J}_{\boldsymbol{\tau}\boldsymbol{\tau}}^{-1} \mathbf{J}_{\mathbf{u}\boldsymbol{\tau}}^{-1} & \mathbf{S}_{\boldsymbol{\tau}}^{-1} \end{bmatrix}, \quad (8)$$

where $\mathbf{S}_{\boldsymbol{\tau}}$ and $\mathbf{S}_{\mathbf{u}}$ are the Schur complements of the submatrix regarding $\boldsymbol{\tau}$ and \mathbf{u} respectively, namely,

$$\mathbf{S}_{\boldsymbol{\tau}} = \mathbf{J}_{\boldsymbol{\tau}\boldsymbol{\tau}} - \mathbf{J}_{\mathbf{u}\boldsymbol{\tau}}^T \mathbf{J}_{\mathbf{u}\mathbf{u}}^{-1} \mathbf{J}_{\mathbf{u}\boldsymbol{\tau}}, \quad (9)$$

$$\mathbf{S}_{\mathbf{u}} = \mathbf{J}_{\mathbf{u}\mathbf{u}} - \mathbf{J}_{\mathbf{u}\boldsymbol{\tau}} \mathbf{J}_{\boldsymbol{\tau}\boldsymbol{\tau}}^{-1} \mathbf{J}_{\mathbf{u}\boldsymbol{\tau}}^T. \quad (10)$$

It can be shown that for multi-image registration, $\mathbf{S}_{\boldsymbol{\tau}}^{-1}$ is given by (see Appendix A)

$$\mathbf{S}_{\boldsymbol{\tau}}^{-1} = \sigma^2 [\mathbf{I}_K + \mathbf{1}\mathbf{1}^T] \otimes \mathbf{Q}^{-1}, \quad (11)$$

where \mathbf{I}_K is the identity matrix of size $K \times K$, $\mathbf{1}$ is a vector of ones of size K , \otimes is the Kronecker product between matrices,

$$\mathbf{Q} = \begin{bmatrix} \mathbf{u}_x^T \mathbf{u}_x & \mathbf{u}_x^T \mathbf{u}_y \\ \mathbf{u}_x^T \mathbf{u}_y & \mathbf{u}_y^T \mathbf{u}_y \end{bmatrix}, \quad (12)$$

and \mathbf{u}_x , \mathbf{u}_y are the derivatives of the latent image \mathbf{u} in the horizontal and vertical directions respectively.

Equation (5) gives a bound on the covariance matrix of any unbiased estimator of $\boldsymbol{\theta}$. Therefore, from (5) and (8), the

MSE of the estimated translations is bounded by the trace of \mathbf{S}_τ^{-1} [43],

$$\text{MSE} = \frac{1}{2K} \sum_{j=1}^K \mathbb{E}[(\tau_{j_x} - \hat{\tau}_{j_x})^2 + (\tau_{j_y} - \hat{\tau}_{j_y})^2] \quad (13)$$

$$\geq \frac{1}{2K} \text{tr}(\mathbf{S}_\tau^{-1}) \quad (14)$$

$$= \sigma^2 \frac{(\mathbf{u}_x^T \mathbf{u}_x + \mathbf{u}_y^T \mathbf{u}_y)}{(\mathbf{u}_x^T \mathbf{u}_x)(\mathbf{u}_y^T \mathbf{u}_y) - (\mathbf{u}_x^T \mathbf{u}_y)^2}. \quad (15)$$

Hence, we define the CRB under a deterministic image model (CRBD) as,

$$\text{CRBD} \stackrel{\text{def}}{=} \sigma^2 \frac{(\mathbf{u}_x^T \mathbf{u}_x + \mathbf{u}_y^T \mathbf{u}_y)}{(\mathbf{u}_x^T \mathbf{u}_x)(\mathbf{u}_y^T \mathbf{u}_y) - (\mathbf{u}_x^T \mathbf{u}_y)^2}. \quad (16)$$

According to the CRBD, the registration error is proportional to the noise level and inversely proportional to the energy of the gradient. A similar result is presented by Robinson and Milanfar [3], who derived the CRB for the super-resolution problem. Multi-image registration can be seen as a particular case of the super-resolution problem, where the under-sampling operator is equal to the identity matrix.

Performance independence of K . An unexpected result is that the bound (16) does not depend on the number of images K . This means that this fundamental limit of multi-image registration performance is the same for a set of 2 or any number K of images. Nevertheless, unlike stated in [3, Ap. III], this does not imply that registration can be done pairwise without loss of information. The CRB gives a lower bound on performance but it does not ensure the existence of an efficient estimator that reaches this bound. In practice, depending on the problem, the CRB may or may not be tight. Hence, the independence of the CRB of the number of images K , does not imply that registration can be done pairwise without loss of information.

As it will be shown experimentally in Section VI, for the multi-image registration problem, the CRBD is tight in high SNR conditions, where we observe indeed that registration can be done pairwise without loss of accuracy. However, it is not necessarily tight in low SNR conditions. In that case, there are other bounds, which are dependent on K , that are closer to the actual performance estimators can achieve.

Case with known underlying image. The bound on (16) corresponds to the translations estimate error when the real image \mathbf{u} is unknown, which is usually the case in practice. In previous works [19], [20], however, the CRB has been computed for the pairwise image registration problem when the only unknown parameters are the shift values.

In that case, the FIM for the multi-image registration problem (7) simplifies to

$$\mathbf{J}_{D_{\text{kn}}} = \mathbf{J}_{\tau\tau} = \frac{1}{\sigma^2} \mathbf{I}_K \otimes \mathbf{Q}, \quad (17)$$

and the CRB for the case where \mathbf{u} is known becomes,

$$\text{CRBD}_{\text{kn}} \stackrel{\text{def}}{=} \frac{1}{2K} \text{tr}(\mathbf{J}_{\tau\tau}^{-1}) \quad (18)$$

$$= \frac{\sigma^2}{2} \frac{(\mathbf{u}_x^T \mathbf{u}_x + \mathbf{u}_y^T \mathbf{u}_y)}{((\mathbf{u}_x^T \mathbf{u}_x)(\mathbf{u}_y^T \mathbf{u}_y) - (\mathbf{u}_x^T \mathbf{u}_y)^2)} = \frac{\text{CRBD}}{2}. \quad (19)$$

Therefore, the MSE bound, assuming the underlying image \mathbf{u} is known, is half that of the case when \mathbf{u} is unknown. When \mathbf{u} is known, and the first image in the set is assumed to be aligned (i.e., $\tau_0 = 0$), all the other images can be pairwise aligned to the known reference. Indeed, in that case, the different observed images are conditionally independent given the known underlying image. Hence, there is no gain in using the rest of the images for estimating the translation of one image. Therefore, the limiting factor in the pairwise alignment is the noise in one image.

On the other hand, when \mathbf{u} is unknown, the bound doubles. This may represent a best case scenario where the limiting factor is twice the noise, corresponding to the pairwise alignment of two noisy images.

B. Bayesian Cramér-Rao with prior on shifts

A natural question that arises after finding that the fundamental performance limit given by the CRBD (16) does not depend on the number of images, is whether this limit can be improved if some prior information about the shifts is known. Intuitively, having more images could improve the alignment performance in the case that \mathbf{u} is unknown. Let us imagine the case of an algorithm that uses an estimation of the latent image \mathbf{u} to estimate the shifts. One could expect that the estimation of \mathbf{u} could be improved by having more images, for example by reducing the noise, and thus leading to a better estimate of the shifts.

Hence, the question is what happens if the motion estimation can be improved by including prior knowledge on the shift vectors. A typical assumption is that the shifts are independent and drawn from a uniform distribution within a limited range. Nevertheless, in some particular applications (e.g., in microscopy or in burst photography), each shift vector depends on the previous ones so modeling the motion as a random walk might be more accurate. In this work, we restrict the analysis to the case where the shifts are independent.

A Bayesian version of the CRB bound can be computed to include prior information on the unknown parameters. The Bayesian Cramér-Rao bound (BCRB) gives a lower bound on the expected error correlation matrix under the joint data and parameter distribution

$$\bar{\mathbf{R}}_\epsilon \geq \mathbf{J}_B^{-1}, \quad (20)$$

where \mathbf{J}_B is the Bayesian Fisher information matrix given by

$$\{\mathbf{J}_B\}_{i,j} = -\mathbb{E}_{\mathbf{z},\boldsymbol{\theta}} \left[\frac{\partial^2 \ell(\mathbf{z}, \boldsymbol{\theta})}{\partial \theta_i \partial \theta_j} \right], \quad (21)$$

and $\ell(\mathbf{z}, \boldsymbol{\theta}) = \log(p(\mathbf{z}, \boldsymbol{\theta}))$ is the logarithm of the joint likelihood function.

Generalized Gaussian prior on shifts. Let us consider a centered generalized Gaussian prior distribution for each component of $\boldsymbol{\tau}$. This family of densities, indexed by the parameters $c > 0$ and $\delta > 0$, is given by

$$p(\boldsymbol{\tau}; c, \delta) = \frac{c \eta(\delta, c)}{\Gamma(1/c) \exp(-\eta^c(c, \delta) |\boldsymbol{\tau}|^c)}, \quad (22)$$

where

$$\eta(\delta, c) = \frac{1}{\delta} \left(\frac{\Gamma(3/c)}{\Gamma(1/c)} \right)^{1/2}, \quad (23)$$

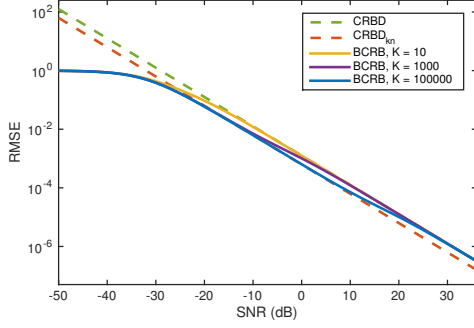


Figure 1: Comparison of the CRBD (both for \mathbf{u} known and unknown) and the BCRB for different number of images K with a Gaussian prior ($c = 2$) with $\delta = 1$ on the shifts.

and Γ denotes the gamma function. The case of $c = 2$ corresponds to the Gaussian density, while the distribution approaches the uniform density with variance δ^2 as $c \rightarrow \infty$.

Given $(K + 1)$ independent samples following model (2), and assuming that \mathbf{u} is an unknown deterministic image and $\boldsymbol{\tau}$ is a random variable following the generalized Gaussian prior (22), the Bayesian FIM is given by (see Appendix B)

$$\mathbf{J}_B = \mathbf{J}_D + \mathbf{J}_p, \quad (24)$$

with

$$\mathbf{J}_p = \begin{bmatrix} 0 & 0 \\ 0 & \frac{1}{\lambda^2} \mathbf{I}_{2K} \end{bmatrix}, \quad (25)$$

where $\lambda^2 = \frac{\delta^2 \Gamma^2(1/c)}{c^2 \Gamma(3/c) \Gamma(2-1/c)}$ and \mathbf{J}_D is the FIM given in (7). Therefore, including a prior on the translations adds the term \mathbf{J}_p to the classical FIM given in (7).

Then, the Schur complement of the submatrix regarding $\boldsymbol{\tau}$, becomes (see Appendix B)

$$\bar{\mathbf{S}}_{\boldsymbol{\tau}} = \frac{1}{\sigma^2} (\mathbf{I} - (K + 1) \mathbf{1} \mathbf{1}^T) \otimes \mathbf{Q} + \frac{1}{\lambda^2} \mathbf{I}, \quad (26)$$

and

$$\begin{aligned} \bar{\mathbf{S}}_{\boldsymbol{\tau}}^{-1} &= \mathbf{I} \otimes \left(\frac{1}{\sigma^2} \mathbf{Q} + \frac{1}{\lambda^2} \mathbf{I} \right)^{-1} \\ &+ \mathbf{1} \mathbf{1}^T \otimes \lambda^2 \left((K + 2) \mathbf{I} + \frac{\lambda^2}{\sigma^2} \mathbf{Q} + (K + 1) \frac{\sigma^2}{\lambda^2} \mathbf{Q}^{-1} \right)^{-1}. \end{aligned} \quad (27)$$

The EMSE of the translations under the given prior is then lower bounded by

$$\text{EMSE} \geq \text{BCRB} \stackrel{\text{def}}{=} \frac{1}{2K} \text{tr}(\bar{\mathbf{S}}_{\boldsymbol{\tau}}^{-1}). \quad (28)$$

As a first observation, let us point out that adding prior information on the translations makes the bound dependent on the number of images K . Figure 1 shows a comparison of the CRB (\mathbf{u} known and unknown) and the BCRB for different number of images K with a Gaussian prior ($c = 2$) with $\delta = 1$. Note that both bounds are very similar for high SNR values. This means that if the SNR is high enough, there is no gain in having prior knowledge about the shifts. However, for low enough SNR and large enough K , the prior bounds the errors on the shift estimates and the BCRB is below the CRBD and approaches the bound for a known image CRBD_{kn} until it reaches a steady-state value equal to the variance of the prior.

Notice that the example shown in Figure 1 corresponds to a pretty tight prior ($\delta = 1$), meaning that an accurate interval

for the shifts is known a priori. Remarkably, even under this seemingly favorable condition, the reduction of the BCRB is observed only for a very low SNR range and for a very large number of images. This suggests a very limited impact of this shift prior in practice, being useful only for very low SNR conditions, a tight prior of the shifts interval, and a very large number of images.

The generalized Gaussian prior approaches the uniform distribution when $c \rightarrow \infty$. Thus, for any fixed δ , $\lambda \rightarrow 0$ as the shift prior approaches a uniform distribution. Hence, the prior information becomes irrelevant and the performance is bounded by the CRBD, which is independent of K . Of course, this does not mean that having more images does not help for estimating the shifts. As previously mentioned, if the CRBD is overoptimistic and cannot be attained, a tighter bound may still exist, that does depend on the number of images.

IV. PERFORMANCE BOUNDS: STOCHASTIC IMAGE MODEL

In this section, we consider a zero-mean Gaussian stochastic model for the underlying unknown image \mathbf{u} . As stated before, our goal is to estimate the K shifts between every pair of $K + 1$ images given by (2), or equivalently in the Fourier domain, from

$$\tilde{z}_i(\boldsymbol{\omega}) = \tilde{u}(\boldsymbol{\omega}) e^{-i\boldsymbol{\omega} \cdot \boldsymbol{\tau}_i} + \tilde{n}_i(\boldsymbol{\omega}), \quad i = 0, \dots, K, \quad (29)$$

where \sim denotes 2D image Fourier transforms, $\boldsymbol{\omega} = [\omega_x, \omega_y]^T$ represents the 2D Fourier spatial frequency and \cdot denotes the inner product operation.

We now assume that the signal samples \mathbf{u} are drawn from a stationary zero-mean Gaussian process with spectral density $S(\boldsymbol{\omega})$. The additive noise is modeled by the zero-mean Gaussian process \mathbf{n}_i with spectral density $N(\boldsymbol{\omega})$, assumed to be independent of the underlying signal \mathbf{u} .

The observed digital images \mathbf{z}_i can be converted into the Fourier domain \tilde{z}_i by applying the 2D DFT. In practice, since the input images are real, the complex Fourier coefficients have Hermitian symmetry, where two of the four quadrants fully determine \tilde{z}_i . Here, we arbitrarily choose to work with the positive values of ω_y and the complete range for ω_x (i.e., first and second quadrants of the 2D DFT). Hence, we will only consider the complex Fourier coefficients corresponding to frequencies $\boldsymbol{\omega}_{l_x, l_y} = [\omega_{l_x}, \omega_{l_y}]^T$ with $\omega_{l_x} = \frac{2\pi l_x}{m_c}$, $l_x = -\frac{m_c}{2}, \dots, \frac{m_c}{2}$ and $\omega_{l_y} = \frac{2\pi l_y}{m_r}$, $l_y = 0, \dots, \frac{m_r}{2}$. In addition, we will assume that the Fourier coefficients of \mathbf{u} are uncorrelated at the considered spatial frequencies.

Let $l(l_x, l_y) = 1, \dots, M$, with $M = m_c + \frac{m_r}{2} + 2$, index all the considered 2D frequencies $\boldsymbol{\omega}_l$. The Fourier transform of the $(K + 1)$ observed images can be arranged into a vector

$$\tilde{\mathbf{z}} = [\tilde{z}_0(\boldsymbol{\omega}_1), \tilde{z}_1(\boldsymbol{\omega}_1), \dots, \tilde{z}_K(\boldsymbol{\omega}_1), \dots, \tilde{z}_0(\boldsymbol{\omega}_M), \tilde{z}_1(\boldsymbol{\omega}_M), \dots, \tilde{z}_K(\boldsymbol{\omega}_M)]^T. \quad (30)$$

Under Gaussian assumptions for the noise and the underlying image, $\tilde{\mathbf{z}}$ follows a complex Gaussian distribution with zero mean and covariance matrix

$$\boldsymbol{\Sigma} = \mathbb{E}[\tilde{\mathbf{z}} \tilde{\mathbf{z}}^H] = \begin{bmatrix} \boldsymbol{\Sigma}_{\boldsymbol{\tau}}(\boldsymbol{\omega}_1) & 0 & \dots & 0 \\ 0 & \boldsymbol{\Sigma}_{\boldsymbol{\tau}}(\boldsymbol{\omega}_2) & \dots & 0 \\ \vdots & \vdots & \ddots & \vdots \\ 0 & 0 & \dots & \boldsymbol{\Sigma}_{\boldsymbol{\tau}}(\boldsymbol{\omega}_M) \end{bmatrix}, \quad (31)$$

where each matrix $\Sigma_{\tau}(\omega)$ has size $(K+1) \times (K+1)$ and is composed by

$$\Sigma_{\tau}(\omega) = \begin{bmatrix} S(\omega) + N(\omega) & S(\omega)e^{-i\tau_1 \cdot \omega} & \dots & S(\omega)e^{-i\tau_K \cdot \omega} \\ S(\omega)e^{i\tau_1 \cdot \omega} & S(\omega) + N(\omega) & \dots & S(\omega)e^{i(\tau_1 - \tau_K) \cdot \omega} \\ \vdots & \vdots & \ddots & \vdots \\ S(\omega)e^{i\tau_K \cdot \omega} & S(\omega)e^{-i(\tau_1 - \tau_K) \cdot \omega} & \dots & S(\omega) + N(\omega) \end{bmatrix}. \quad (32)$$

A. Cramér-Rao lower bound: stochastic image model

In order to compute the CRB for the shifts estimation in the multi-image alignment problem under model (2), we first compute the corresponding FIM matrix. For the considered complex Gaussian process $\hat{\mathbf{z}}$, it is given by [18, Ap. 15C]

$$\{\mathbf{J}_S\}_{i_h, j_q} = \text{tr} \left(\Sigma^{-1} \frac{\partial \Sigma}{\partial \tau_{i_h}} \Sigma^{-1} \frac{\partial \Sigma}{\partial \tau_{j_q}} \right), \quad (33)$$

where $i, j = 1, \dots, K$, and $h, q \in \{x, y\}$ index the two components of each 2D shift vector $\tau_i = [\tau_{i_x}, \tau_{i_y}]^T$. Carrying out the indicated operations (see Appendix C) we get

$$\mathbf{J}_S = [(K+1)\mathbf{I}_K - \mathbf{1}\mathbf{1}^T] \otimes \mathbf{B}, \quad (34)$$

with

$$\mathbf{B} = \begin{bmatrix} \rho_{x,x} & -\rho_{x,y} \\ -\rho_{x,y} & \rho_{y,y} \end{bmatrix}, \quad (35)$$

and

$$\rho_{h,q} = \sum_{l=1}^M \frac{2S^2(\omega_l) \omega_{l_h} \omega_{l_q}}{N^2(\omega_l) + (K+1)S(\omega_l)N(\omega_l)}. \quad (36)$$

Hence, we have

$$\mathbf{J}_S^{-1} = \frac{1}{(K+1)} [\mathbf{I}_K + \mathbf{1}\mathbf{1}^T] \otimes \mathbf{B}^{-1}. \quad (37)$$

The error covariance matrix of any unbiased estimate of the shifts is thus bounded by

$$\mathbb{E}_{\mathbf{z}|\tau}[(\hat{\tau} - \tau)(\hat{\tau} - \tau)^T] \geq \mathbf{J}_S^{-1}, \quad (38)$$

and the MSE is lower bounded by the trace of \mathbf{J}_S^{-1} ,

$$\text{MSE} \geq \frac{1}{2K} \text{tr}(\mathbf{J}_S^{-1}) = \frac{1}{(K+1)} \left(\frac{\rho_{x,x}^2 + \rho_{y,y}^2}{\rho_{x,x}\rho_{y,y} - \rho_{x,y}^2} \right). \quad (39)$$

If $S(\omega)$ and $N(\omega)$ are rotationally symmetric (i.e., rotation invariant), it can be shown that $\rho_{x,y} = 0$ and $\rho_{x,x} = \rho_{y,y}$. In this case, we define the CRB under the Gaussian stochastic image model (CRBS) as

$$\text{CRBS} \stackrel{\text{def}}{=} \frac{2}{(K+1)\rho_{x,x}} = \frac{2}{(K+1)\rho_{y,y}}. \quad (40)$$

Notice that, unlike the CRBD (16), the CRBS (40) depends on the number of images K .

High SNR. Under high signal-to-noise conditions, the CRBS for a rotation invariant process (40) simplifies to

$$\text{CRBS}^{\text{HSNR}} \stackrel{\text{def}}{=} \frac{2\sigma^2(2\pi)^2}{N_p \int S(\omega) \omega_x^2 d\omega}. \quad (41)$$

This bound is indeed independent of the number of images K and agrees with the deterministic CRB given by (16) (see Appendix C).

To help further understand the behavior of the computed bound we analyze its behavior both for natural and flat spectrum images.

Natural images. A typical natural image presents complex structure that is difficult to model accurately. One classical assumption, it that the power spectrum of natural images falls quadratically with the Fourier frequency. Although simplistic, this is in fact reasonable if we consider that natural images have a relative contrast energy that is scale invariant [44]. Let us assume that the considered underlying image follows this law, that is,

$$S(\omega) = \begin{cases} S_n \|\omega\|^{-2} & \text{if } \max(|\omega_x|, |\omega_y|) \leq W/2, \\ 0 & \text{otherwise,} \end{cases} \quad (42)$$

where S_n is a known parameter, and $W \in (0, 2\pi]$ models the signal bandwidth. Also, we will assume that the additive noise spectrum has a constant value N in the frequency band $[-\frac{W}{2}, \frac{W}{2}]^2$ and is zero otherwise.

Let us define the signal-to-noise ratio as the ratio between the energy of the derivative and the noise power

$$\text{SNR} \stackrel{\text{def}}{=} \frac{1}{NW^2} \int S(\omega) \|\omega\|^2 d\omega. \quad (43)$$

For the case of a natural image (42), the SNR is then

$$\text{SNR}_n = S_n/N. \quad (44)$$

and the CRBS bound for natural images becomes (see Appendix C)

$$\text{CRBS}_n \stackrel{\text{def}}{=} \frac{8\pi}{N_p(K+1)\text{SNR}_n^2 \text{acoth}\left(1 + \frac{2\pi(K+1)\text{SNR}_n}{W^2}\right)}. \quad (45)$$

When $\text{SNR}_n \rightarrow \infty$, we have that

$$\text{CRBS}_n \rightarrow \frac{16\pi^2}{N_p W^2 \text{SNR}_n}, \quad (46)$$

which does not depend on K . The breaking point from the asymptotic (very high SNR point) occurs approximately when $2\pi(K+1)\text{SNR}_n \approx W^2$, which happens at,

$$\text{SNR}_{n1}^K = \frac{W^2}{2\pi(K+1)}. \quad (47)$$

This implies that, if $\text{SNR}_n \gg \text{SNR}_{n1}^{K=1}$, having access to more than two images will not improve the bound. This absolute breaking point happens at approximately $\text{SNR}_{n1} \stackrel{\text{def}}{=} \frac{1}{5} \frac{W^2}{4\pi}$.

Flat spectrum images. Another helpful case is to study the behavior of the CRBS when the underlying signal u has a flat power spectral density, that is,

$$S(\omega) = \begin{cases} S_w & \text{if } \max(|\omega_x|, |\omega_y|) \leq W/2, \\ 0 & \text{otherwise.} \end{cases} \quad (48)$$

Similarly, we assume that the additive noise spectrum $N(\omega)$ has a constant value of N in the frequency band $[-\frac{W}{2}, \frac{W}{2}]^2$ and is zero otherwise.

The signal-to-noise ratio (as defined in (43)) for white signals becomes

$$\text{SNR}_w = \frac{S_w W^2}{6N}. \quad (49)$$

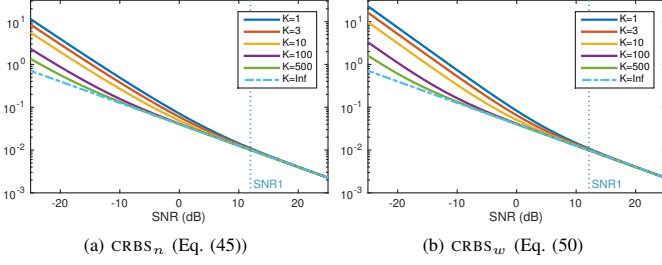


Figure 2: Comparison of CRBS for different number of input images K and varying SNR conditions. (a) natural image model, (b) flat spectrum image. Both image models have very similar behavior.

In this case, the CRB bound for flat spectrum images is (see Appendix C)

$$\begin{aligned} \text{CRBS}_w &\stackrel{\text{def}}{=} \frac{8\pi^2 (W^2 + 6\text{SNR}_w(K+1))}{3N_p(K+1)\text{SNR}_w^2 W^2} \\ &= \frac{8\pi^2}{3N_p(K+1)\text{SNR}_w^2} + \frac{16\pi^2}{N_p W^2 \text{SNR}_w}. \end{aligned} \quad (50)$$

In particular, when $\text{SNR}_w \rightarrow \infty$ we have

$$\text{CRBS}_w \rightarrow \frac{16\pi^2}{N_p W^2 \text{SNR}_w}, \quad (51)$$

which does not depend on the number of images K . The breaking point is when both terms in (50) are approximately equal, which happens at

$$\text{SNR}_{w1}^K = \frac{W^2}{6(K+1)}. \quad (52)$$

Thus, if $\text{SNR}_w \gg \text{SNR}_{w1}^{K=1}$, having access to more than two images will not improve the bound. This absolute breaking point happens at approximately $\text{SNR}_{w1} \stackrel{\text{def}}{=} \frac{1}{5} \frac{W^2}{12}$.

Because this threshold is very similar to the one obtained for natural images (see Eq. (47)), for simplicity, we refer hereafter to both SNR_{n1} and SNR_{w1} as SNR_1 .

Figure 2 shows the computed CRBS bounds for both image models, with different number of input images K and varying SNR levels. Both image models have very similar behavior. There is a very high SNR zone where the bounds depend linearly with the SNR level ($\text{SNR} > \text{SNR}_1$). Within this SNR region, having access to more images does not have an impact on the bound. In moderate to low SNRs ($\text{SNR} < \text{SNR}_1$) both Cramér-Rao stochastic bounds depend super-linearly with the SNR (i.e., performance degrades faster at low SNR values than in the very high SNR region). Increasing the number of images pushes back SNR_1 , increasing the SNR range where performance is linear with SNR. The performance is linear with image size N_p in both cases on the whole SNR domain.

An alternative approach to include an image model is to compute a Hybrid Cramér-Rao bound (HCRB).² Similarly to what was done in Section III-B, one can compute a HCRB including the desired model as an image prior and then compute the expected FIM under this prior. Robinson and Milanfar [3] computed such bound for the super-resolution

problem assuming a Gaussian model for the image similar to the one presented here. Although related, these two bounds are different. The HCRB gives a bound on the expected MSE under the given image prior. This can be seen as an average bound for the different likelihoods obtained for each given possible value of the image. On the other hand, the CRB on Equation (40) gives the bound based on the expected likelihood under the given image model. Under some regularity conditions, it is possible to show that the CRB is always tighter than the HCRB [45, Thm. 1]. Nevertheless, in many applications the computation of the HCRB is much simpler than the CRB, leading to a reasonable alternative.

B. Extended Ziv-Zakai lower bound

In general, the CRB is known to be tight in high SNR but overoptimistic in low SNR conditions. Various Bayesian bounds have been derived to obtain tighter and more accurate predictions of the MSE behavior in the entire SNR range. One example of this is the bound proposed by Ziv and Zakai [23], which relates the expected MSE (EMSE) of the estimator over a given prior, to the probability of error in a binary detection problem.

Consider the estimation of a $2K$ -dimensional random vector θ with a prior distribution p_θ , based upon an observation vector \mathbf{z} . The extended Ziv-Zakai lower bound (EZZB) on the EMSE of any estimate $\hat{\theta}$ of θ over p_θ is given by [26]

$$\mathbf{a}^T \bar{\mathbf{R}}_\epsilon \mathbf{a} \geq \int_0^\infty \mathcal{V} \left\{ \max_{\delta: \mathbf{a}^T \delta = h} \left[\int_{\mathbb{R}^K} \min(p_\theta(\varphi), p_\theta(\varphi + \delta)) \cdot P_{\min}(\varphi, \varphi + \delta) d\varphi \right] \right\} h dh, \quad (53)$$

where \mathbf{a} is any $2K$ -dimensional vector, $\mathcal{V}\{\cdot\}$ is the valley-filling function,³ and $P_{\min}(\delta)$, $\delta \in \mathbb{R}^{2K}$, is the probability of error in the binary detection problem

$$H_0 : \hat{\delta} = \varphi; \mathbf{z} \sim p(\mathbf{z} | \theta = \varphi), \quad (54)$$

$$H_1 : \hat{\delta} = \varphi + \delta; \mathbf{z} \sim p(\mathbf{z} | \theta = \varphi + \delta), \quad (55)$$

with equally likely hypotheses. The vector $\delta = [\delta_1, \dots, \delta_K]$, with $\delta_i = [\delta_{ix}, \delta_{iy}]^T$ represents a possible 2D shift between the i -th and the first image (indexed in the same way as τ).

The Ziv-Zakai bound is based on the probability of correctly choosing the parameter to be estimated between two possible values: φ or $\varphi + \delta$. The bound is found by integrating the minimum error along all possible estimated values (in general ruled by both δ and φ), weighted by their prior probability of occurrence, and by bounding the minimum probability of error in this binary detection problem.

If the probability of error is only a function of the offset between the hypothesis, i.e., $P_{\min}(\varphi, \varphi + \delta) = P_{\min}(\delta)$, which is precisely the case in our translation estimation problem, the bound simplifies to

$$\mathbf{a}^T \bar{\mathbf{R}}_\epsilon \mathbf{a} \geq \int_0^\infty \mathcal{V} \left\{ \max_{\delta: \mathbf{a}^T \delta = h} A(\delta) P_{\min}(\delta) \right\} h dh, \quad (56)$$

³The valley-filling of a function $f(h)$ is obtained by filling-in any valleys [26], and is given by $\mathcal{V}\{f\}(h) = \max_{t \geq 0} f(h+t)$.

²Hybrid in the sense that there are random and deterministic parameters.

where

$$A(\boldsymbol{\delta}) = \int_{\mathbb{R}^{2K}} \min(p_{\boldsymbol{\theta}}(\boldsymbol{\varphi}), p_{\boldsymbol{\theta}}(\boldsymbol{\varphi} + \boldsymbol{\delta})) d\boldsymbol{\varphi}. \quad (57)$$

Thus, to compute the EZZB of the shift estimation problem we need to compute $A(\boldsymbol{\delta})$ and the probability of error $P_{\min}(\boldsymbol{\delta})$.

If we assume the shifts $\boldsymbol{\theta}$ to be uniformly distributed $\boldsymbol{\theta} \sim \mathcal{U}[0, D]^{2K}$, $A(\boldsymbol{\delta})$ takes the simplified form

$$A(\boldsymbol{\delta}) = \prod_{i=1}^{2K} \left(1 - \frac{\delta_i}{D}\right). \quad (58)$$

The probability of error $P_{\min}(\boldsymbol{\delta})$ for the case of multi-image registration is given by (see Appendix D)

$$P_{\min}(\boldsymbol{\delta}) \approx \frac{1}{2} \exp\{a(\boldsymbol{\delta}) + b(\boldsymbol{\delta})\} \Phi\left(\sqrt{2b(\boldsymbol{\delta})}\right), \quad (59)$$

where

$$a(\boldsymbol{\delta}) = -\sum_{l=1}^M \log[1 + \gamma(\boldsymbol{\delta}, \boldsymbol{\omega}_l)], \quad b(\boldsymbol{\delta}) = \sum_{l=1}^M \frac{\gamma(\boldsymbol{\delta}, \boldsymbol{\omega}_l)}{1 + \gamma(\boldsymbol{\delta}, \boldsymbol{\omega}_l)}, \quad (60)$$

$$\gamma(\boldsymbol{\omega}, \boldsymbol{\delta}) = \frac{S(\boldsymbol{\omega})^2 \left((K+1)^2 - T(\boldsymbol{\delta}, \boldsymbol{\omega})\right)}{4(N(\boldsymbol{\omega})^2 + (K+1)N(\boldsymbol{\omega})S(\boldsymbol{\omega}))}, \quad (61)$$

$$T(\boldsymbol{\delta}, \boldsymbol{\omega}) = \left|1 + \sum_{j=1}^K e^{-i\boldsymbol{\delta}_j \cdot \boldsymbol{\omega}}\right|^2 \quad \text{and} \quad \Phi(t) = \frac{1}{\sqrt{2\pi}} \int_t^\infty e^{-\frac{t^2}{2}} dt. \quad (62)$$

Flat spectrum signals. As done for the CRBS case, let us consider the particular case of flat spectrum signals defined previously by Equation (48). The analysis presented hereafter closely follows and extends the work by Weinstein and Weiss [29] to the case of multiple signals.

For simplicity, the following analysis is restricted to one-dimensional signals. The extension to two-dimensional signals is straightforward in the case where the image is assumed to be drawn from a white random process (full bandwidth flat spectrum, i.e., $W = 2\pi$). In this case, knowing the translation in one direction does not give any additional information to the estimation of the other one. As a consequence, the 2D image can be rearranged into a one-dimensional vector by concatenating its rows without loss of information regarding the estimation of the translation along the columns. Following this remark, in this section, we will consider one-dimensional signals having length $N_p = m_r \times m_c$ and $W = 2\pi$.

The EZZB corresponding to the estimation of one single component is given by (see Appendix E)

$$\text{EMSE}_1 \geq \text{EZZB}_w \stackrel{\text{def}}{=} \frac{1}{c^2} \int_0^{\sqrt{2b}} h \exp\left\{-\frac{9h^4}{20N_p}\right\} \Phi(h) dh + \frac{D^2}{6} e^{a+b} \Phi(\sqrt{2b}), \quad (63)$$

where

$$a = -N_p \log\left(\frac{\sqrt{\kappa_2+1}+1}{2}\right), \quad b = \frac{N_p}{2} \frac{\sqrt{\kappa_2+1}-1}{\sqrt{\kappa_2+1}}, \quad c^2 = \frac{N_p \pi^2 \kappa_1}{12} \\ \kappa_1 = \frac{9\text{SNR}_w^2(K+1)}{8\pi^4 + 12\pi^2 \text{SNR}_w(K+1)}, \quad \kappa_2 = \frac{9\text{SNR}_w^2 K}{4\pi^4 + 6\pi^2 \text{SNR}_w(K+1)}. \quad (64)$$

Analysis of the EZZB: different SNR regions. The EZZB behaves differently in low and high SNR regimes, as dictated by the two terms in Eq. (63) and as illustrated in Figure 3(a).

i) High SNR. For $\text{SNR}_w \gg 1$, the error term (63) is mainly driven by the first term since $a + b \rightarrow -\infty$ and $b \rightarrow \frac{N_p}{2}$.

Assuming that $N_p \gg 1$, we obtain [28]

$$\text{EZZB}_w \xrightarrow{\text{SNR}_w \rightarrow \infty} \frac{1}{c^2} \int_0^{\sqrt{2b}} h \cdot \exp\left\{-\frac{9h^4}{20N_p}\right\} \Phi(h) dh \quad (65)$$

$$\approx \frac{1}{c^2} \int_0^\infty h \cdot \exp\left\{-\frac{9h^4}{20N_p}\right\} \Phi(h) dh = \frac{1}{4c^2} \quad (66)$$

$$= \frac{8\pi^2 + 12\text{SNR}_w(K+1)}{3N_p \text{SNR}_w^2(K+1)} = \text{CRBS}_w. \quad (67)$$

Indeed, in the high SNR regime, the EZZB approaches the CRBS under the stochastic image model given by (50).

ii) Low SNR. On the other hand, in a very low SNR scenario, $\text{SNR}_w \ll 1$, $a \rightarrow 0$, $b \rightarrow 0$ and $c \rightarrow 0$. Thus,

$$\text{EZZB}_w \xrightarrow{\text{SNR}_w \rightarrow 0} \frac{D^2}{6} e^{a+b} \Phi(\sqrt{2b}) \approx \frac{D^2}{12}, \quad (68)$$

which is the variance of the shifts prior.

iii) Transition zone. The transition from the low-SNR to the high-SNR region starts when the two terms have a similar contribution to the bound, that is,

$$\frac{1}{4c^2} = \frac{D^2}{6} e^{a+b} \Phi(\sqrt{2b}). \quad (69)$$

We could (arbitrarily) say that the transition is completed when the bound reaches half the asymptotic value, i.e.,

$$e^{a+b} \Phi(\sqrt{2b}) = \frac{1}{4}. \quad (70)$$

Equations (69) and (70) characterize the limit SNR levels of the transition zone. Let SNR_2 be the SNR level that satisfies (69) and SNR_3 the SNR level satisfying (70). Within this transition region the bound is essentially dominated by the behavior of $\Phi(\sqrt{2b})$.

Figure 3 shows how this region changes when varying the number of images K , the prior D and the image size N_p . The threshold SNR_2 , below which the EMSE decreases significantly and worsens exponentially with the SNR, depends on the number of available images K . This is probably the most important consequence of having access to more images. Figure 3(b) shows how this threshold can be pushed back several dBs by increasing K , until reaching a limit.

Note that this critical SNR level SNR_2 also depends on the image size N_p . As a consequence, increasing the image size reduces the performance bound and pushes this SNR limit as shown in Figure 3(c).

On the other hand, as illustrated in Figure 3(d), the threshold SNR_2 is not significantly affected by the shift prior parameter D . This means that, for practical D values (e.g., $D \geq 1$), having a tighter shift prior does not push back SNR_2 significantly. Nevertheless, as expected, the steady state EMSE predicted by EZZB does decrease with D .

V. COMPARISON OF PERFORMANCE BOUNDS

In this section, we analyze and compare the behavior of the previously computed CRB and EZZB bounds. To this effect, it is important to make the distinction that the CRB is a bound on the MSE while the EZZB and the BCRB are bounds on the EMSE over a given prior for the shifts.

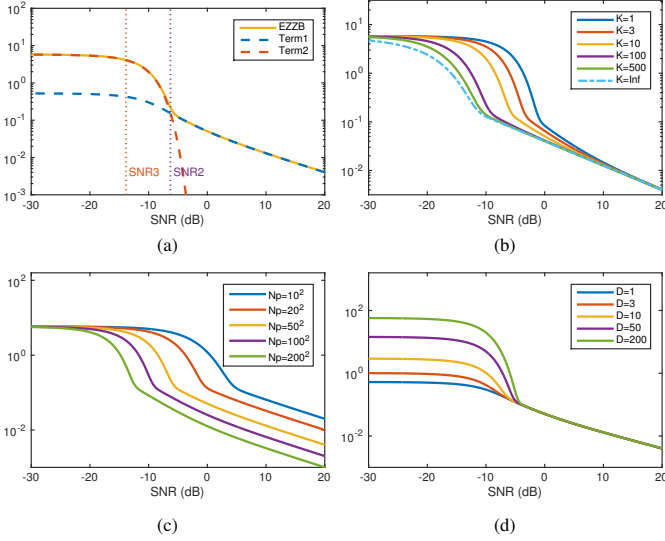


Figure 3: (a) The breaking point of the EZZB bound and its decomposition as the sum of two terms for varying SNR conditions and $K = 10$. Term 1 corresponds to Equation (65) and term 2 corresponds to Equation (68). (b-d) Comparison of EZZB at varying SNR conditions for different number of input images K (b), different image size N_p (c) and different shift prior intervals D (d).

To simplify the discussion, let us consider the case of white signals. Figure 4 shows a comparison of the CRB bounds (both for deterministic (CRBD) and stochastic (CRBS) image models), the BCRB (with Gaussian shift prior of variance $\lambda^2 = 1$) and the EZZB (with uniform $[0, D]$ shift prior, $D = 20$) assuming an image of size 50×50 pixels. For the CRBD and the BCRB cases, that depend on a deterministic signal, we used a realization from the white random process used in CRBS and EZZB. Based on the SNR values, the behavior of the bounds can be characterized into four different regions i-iv.

i) Very high SNR ($\text{SNR} \geq \text{SNR}_1$). In this region, all bounds agree. Hence, the same fundamental limit is predicted for both the MSE and the EMSE. This limit does not depend on the shift value nor on the width of the prior, within practical limits for λ and D ($D, \lambda \geq 1$). The performance bound only depends on the total image gradient energy and the noise level, and it is linear with the SNR and image size N_p . Hence, a very important remark is that, in this SNR region, all bounds predict that having access to more than two images ($K > 1$) or having a more accurate shift priors (a smaller λ or D within practical limits) will not lead to better performance. The threshold defining this region, SNR_1 , depends on the number of images K (see Eq. (52)). It does not depend, however, on the variance of the prior (D, λ) nor the image size (N_p).

ii) High SNR ($\text{SNR}_1 \leq \text{SNR} \leq \text{SNR}_2$). In this region, the CRBS and the EZZB agree, while the CRBD and the BCRB are overoptimistic. The main differences with respect to the very high SNR region is that the CRBS and the EZZB improve with increasing number of images K , and their dependence on the SNR is super-linear. This means that the performance decreases faster when reducing the SNR than in the very high SNR region. In the limit, when $K \rightarrow \infty$, the EZZB and CRBS

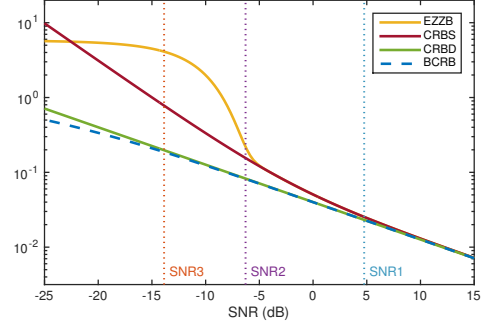


Figure 4: Comparison of the EZZB, CRBS, CRBD and BCRB bounds for $K = 10$ and varying SNR conditions.

approach the CRBD (same behavior as in very high SNR). In this region, performance is linear with image size N_p .

iii) Transition ($\text{SNR}_2 \leq \text{SNR} \leq \text{SNR}_3$). The EZZB predicts a threshold SNR_2 below which the EMSE decreases significantly, and worsens exponentially with the SNR. This critical SNR level can be improved by increasing the number of available images K (up to some limit, see Figure 3(b)) or the image size N_p . Nevertheless, the threshold does not depend considerably on the shift prior D (see Figure 3(d)).

iv) Saturation ($\text{SNR} \leq \text{SNR}_3$). The EZZB predicts a critical SNR below which no alignment is possible, and thus the error is dominated by the shifts prior (the EMSE is essentially given by the variance of the prior).

VI. PERFORMANCE BOUNDS TIGHTNESS ASSESSMENT

The bounds derived in sections III and IV set an upper limit on the best possible performance of any estimator, but there is no guarantee about the existence of an estimator reaching that performance. Therefore, by only looking at the bounds, it is hard to draw practical conclusions about the actual achievable alignment performance in practice. Indeed, there could always exist a tighter bound, with a different behavior than the computed ones, that gets closer to best achievable performance. Hence, assessing the tightness of the derived bounds to the actual alignment performance becomes critical to close this gap.

In what follows, we compare the empirical performance of the maximum likelihood estimator (MLE) to the bounds previously computed. MLE is perhaps the most widely used estimator in statistical parameter estimation problems. It is asymptotically efficient [18], and it is also known to be efficient for any number of samples in various problems [21].

A. Maximum Likelihood Estimation

Given $(K + 1)$ independent samples following Model (2), and assuming \mathbf{u} is an unknown deterministic image, the MLE of $\boldsymbol{\theta} = [\mathbf{u}, \boldsymbol{\tau}]^T$ is the value that maximizes the log-likelihood,

$$[\mathbf{u}, \boldsymbol{\tau}]_{\text{MLE}} = \arg \max_{\mathbf{u}, \boldsymbol{\tau}} - \frac{1}{2\sigma^2} \sum_{i=0}^K \|z_i(\mathbf{x}) - u(\mathbf{x} - \boldsymbol{\tau}_i)\|^2, \quad (71)$$

where we discarded the terms independent of $[\mathbf{u}, \boldsymbol{\tau}]$.

The functional in (71) is an example of a separable non-linear least-square problem. Indeed, given the vector $\boldsymbol{\tau}$ containing all the shifts, the unknown underlying image \mathbf{u} would be given by the least squares solution

$$\hat{\mathbf{u}}(\mathbf{x}) = \frac{1}{(K+1)} \sum_{i=0}^K z_i(\mathbf{x} + \boldsymbol{\tau}_i). \quad (72)$$

That is, given the shift values, the MLE of the unknown image is the average of the aligned frames. Inserting (72) back into (71), the functional to be optimized depends on the shifts only, that is,

$$\boldsymbol{\tau}_{\text{MLE}} = \arg \min_{\boldsymbol{\tau}} \sum_{i=1}^K \|z_i(\mathbf{x}) - \hat{\mathbf{u}}(\mathbf{x} - \boldsymbol{\tau}_i)\|^2, \quad (73)$$

where $\hat{\mathbf{u}}(\mathbf{x})$ is given by (72). Functional (73) is non-convex and different approaches can be followed to find a local minimum [4]. One such approach consists in alternating two steps: first compute the average of the frames aligned with the current estimate of the shifts (given by (72)); second align each image against the current average by choosing the shift that maximizes the Euclidean distance against the average. That is,

$$\hat{\mathbf{u}}^{(t+1)}(\mathbf{x}) = \frac{1}{(K+1)} \sum_{i=0}^K z_i(\mathbf{x} + \boldsymbol{\tau}_i^{(t)}), \quad (74)$$

$$\boldsymbol{\tau}_i^{(t+1)} = \arg \min_{\boldsymbol{\tau}_i} \|z_i - \hat{\mathbf{u}}^{(t+1)}(\mathbf{x} - \boldsymbol{\tau}_i)\|^2. \quad (75)$$

This algorithm requires an initialization either for $\boldsymbol{\tau}$ or $\hat{\mathbf{u}}$. One possibility is to align each input image to a reference image in the set and take those estimated translations as initial values. The algorithm stops when the shifts reach a steady value.

In our implementation, we used image correlation [46] which can be seen as an approximation of the L_2 distance that should be minimized. We initialize the iterative algorithm by aligning each image to the first one in the set, and take those translations as initial values. We refer hereafter to this approximation of the MLE as MLE_{avg} .

B. Experimental analysis

An experimental analysis is conducted in order to compare the performance of the MLE to the previously introduced bounds. For this purpose, synthetic data is generated according to model (2). Two cases are considered for the underlying image \mathbf{u} : a natural image (Figure 5) and a flat spectrum image (a realization of a uniformly distributed random variable). The shifts $\boldsymbol{\tau}_i$ are uniformly sampled in $[-5, 5]^2$. Different noise levels σ^2 and number of images K are evaluated. The performance was computed by averaging the estimation errors over 100 tests for each particular configuration (K, σ^2) .

The squared bias of the MLE_{avg} experiments was on average, in all the conducted experiments, four orders of magnitude smaller than the estimator variance. Hence, we report the root mean squared error (RMSE) of the MLE_{avg} , which is dominated by its variance given that the method is almost unbiased.

Figure 6 shows the results obtained by the MLE_{avg} using as underlying image the ones shown in Figure 5, for different number of input images ($K = 1, 10, 50$) and SNR levels.



Figure 5: Natural images used for the experimental analysis in Section VI. From left to right: building (by M. Colom / CC BY), paris, napoli, bolivia. All images are 256×256 pixels.

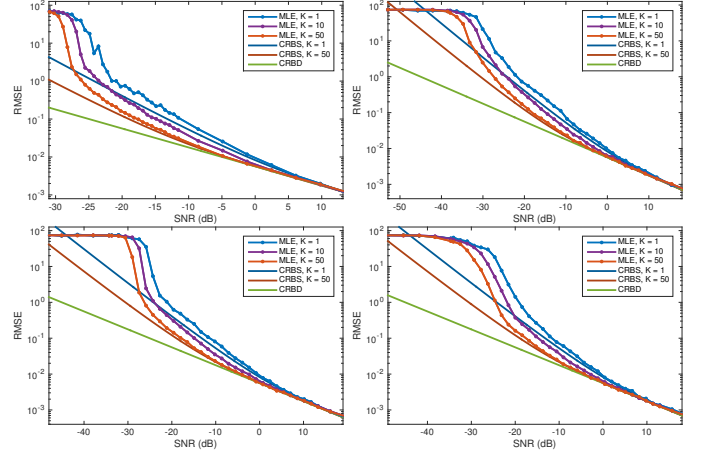


Figure 6: Natural images. Comparison of the MLE performance for different number of images K to the CRB under the deterministic image model (CRBD) and the natural image stochastic model (CRBS) for the four examples shown in Fig. 5: building (top-left), paris (top-right), napoli (bottom-left) and bolivia (bottom-right).

The results are compared to the CRBD (Eq. (16)) and to the CRBS (Eq. (45)) for $K = 10$. Figure 7 shows the results of the MLE_{avg} for $K = 1, 10$ on a flat spectrum underlying image, compared to the CRBS and EZZB. The case $K = 1$ corresponds to pairwise alignment.

For both natural and flat spectrum images, similarly to what was predicted by the EZZB, we identify four different regions of behavior of the MLE_{avg} depending on the SNR value (compare figures 6 and 7 to Figure 4).

For very high SNR, all bounds agree and the MLE_{avg} attains the limiting performance, which is independent of the number of images K . Thus, under very high SNR, the alignment can be performed pairwise without loss of accuracy and MLE is an optimal estimator.

For moderate to high SNR, a different behavior is observed for flat spectrum and natural images. For flat spectrum images, the MLE_{avg} still attains the limiting performance given by the CRBS and is thus optimal. For natural images, on the contrary, the MLE_{avg} performance is close to the CRBS but it is not tight. A possible reason explaining this behavior is the non-optimality of the MLE_{avg} , for which a critical drawback is that it does not use image prior information. Moreover, for this SNR region, the MLE_{avg} performance clearly improves with increasing number of images. Because the CRBS bound for $K = 1$ is outperformed when using more images, we can conclude that pairwise registration is not optimal when more images are available under moderate to high SNR levels (see figures 6 and 7).

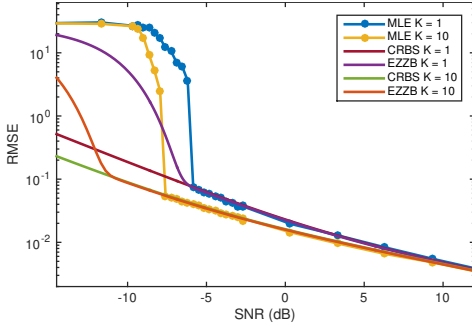


Figure 7: Flat spectrum. Comparison of the MLE performance to the Cramér-Rao bound (CRBS) and the Ziv-Zakai bound (EZZB) for the pairwise and $K = 10$ cases.

Similarly, as predicted by the EZZB for white signals, we observe a transition zone where performance degrades dramatically to finally converge to a flat zone. The flat region corresponds to SNR levels that are too low to enable alignment at all. For flat spectrum images and pairwise alignment ($K = 1$), the EZZB accurately predicts the SNR threshold that defines the beginning of this transition region. However, for the multi-image case ($K = 10$) the MLE_{avg} algorithm performs worse than the prediction given by the EZZB (see Figure 7). One reason for this might be that the initialization of the non-convex optimization in MLE_{avg} is performed using the pairwise registration to one of the input images, which is certainly not optimal. Nevertheless, as predicted by EZZB, the breaking point of the MLE_{avg} is pushed back several dBs when using more images in the registration (see figures 6 and 7).

VII. CONCLUSIONS

In this work, we analyzed the fundamental performance limits in image registration when multiple shifted and noisy observations are available. We derived and analyzed Cramér-Rao and extended Ziv-Zakai bounds under different statistical models for both the underlying image and the shift vectors.

The first clear finding is that there is a *per-region* behavior depending on the difficulty level of the problem, given by the SNR conditions (see for example figures 4 and 7). At very high SNR, the performance is linear with both, the SNR and the image size, and it is independent of the prior information on the shifts and the number of available images. Indeed, all computed bounds agree, and the MLE achieves the bounds. Hence, doing pairwise alignment using the MLE gives the optimal performance.

Assuming a stochastic image model, in high to moderate SNR scenarios, the performance is super-linear with the SNR and linear with the image size. Increasing the number of images widens the region where performance is linear with the SNR (very high SNR), so it improves registration. This is true for both considered stochastic image models: flat power spectral density or with quadratic decay. Also, this agrees with the empirical MLE performance in this SNR range.

According to the computed extended Ziv-Zakai bound, there exists a critical SNR below which performance degrades dramatically with SNR. Having access to more images or

increasing the image size help to push the SNR levels at which this transition zone starts. In very low SNR, the performance saturates to a value essentially given by the prior variance on the shifts. In this SNR region no alignment is possible.

In general, having access to more images improves the performance up to a certain limit. The exception is within the very high SNR region, where pairwise alignment is optimal. Increasing the image size always improves performance, linearly reducing the performance bounds and pushing the critical thresholds delimiting the transition and saturation zones. The studied shifts priors only had an impact at low SNR levels.

As future work, we would like to analyze the impact of having more complex shift priors, for instance modeling correlation between the acquired frames (e.g., modeled by a random walk). In addition, targeting a particular class of images, could help to develop better image priors. This will have an impact on the moderate to low SNR levels, since the performance in high SNR is found to be independent of the image prior. Indeed, MLE_{avg} has proven to be optimal when registering white noise signals (for the considered image size), but suboptimal for natural images in moderate SNR conditions. Prior information could help to close the gap between the fundamental limit and the MLE performance.

ACKNOWLEDGMENTS

Work partially supported by the Department of Defense and NSF. The authors would like to thank Jean-Michel Morel for fruitful comments and discussions. This work is in honor of Prof. Moshe Zakai, he will always be remembered as one of the greatest.

APPENDIX A

CRAMÉR-RAO BOUND: DETERMINISTIC IMAGE MODEL

Let \mathbf{z} be $(K + 1)$ independent samples following (2), and assuming \mathbf{u} is an unknown deterministic image, the log-likelihood function of \mathbf{z} with $\boldsymbol{\theta} = [\mathbf{u}^T, \boldsymbol{\tau}^T]^T$ is given by

$$\ell(\mathbf{z}; \boldsymbol{\theta}) = -\frac{1}{2\sigma^2} \sum_{i=0}^K \|z_i(\mathbf{x}) - u(\mathbf{x} - \boldsymbol{\tau}_i)\|^2, \quad (76)$$

where we discarded the terms independent of $\boldsymbol{\theta}$. To compute the CRB we first compute the FIM

$$\mathbf{J}_D = -\mathbb{E}_{\mathbf{z}|\boldsymbol{\theta}} \left[\frac{\partial^2 \ell(\mathbf{z}; \boldsymbol{\theta})}{\partial \boldsymbol{\theta}^2} \right] = \begin{bmatrix} \mathbf{J}_{\mathbf{uu}} & \mathbf{J}_{\mathbf{u}\boldsymbol{\tau}}^T \\ \mathbf{J}_{\mathbf{u}\boldsymbol{\tau}} & \mathbf{J}_{\boldsymbol{\tau}\boldsymbol{\tau}} \end{bmatrix}. \quad (77)$$

Hence,

$$\mathbf{J}_{\mathbf{uu}} = -\mathbb{E}_{\mathbf{z}|\boldsymbol{\theta}} \left[\frac{\partial^2 \ell(\mathbf{z}; \boldsymbol{\theta})}{\partial \mathbf{u}^2} \right] = \frac{1}{\sigma^2} (K + 1) \mathbf{I}_{N_p}, \quad (78)$$

$$\mathbf{J}_{\boldsymbol{\tau}\boldsymbol{\tau}} = -\mathbb{E}_{\mathbf{z}|\boldsymbol{\theta}} \left[\frac{\partial^2 \ell(\mathbf{z}; \boldsymbol{\theta})}{\partial \boldsymbol{\tau}^2} \right] = \frac{1}{\sigma^2} \mathbf{I}_K \otimes \mathbf{Q}, \quad (79)$$

$$\mathbf{J}_{\mathbf{u}\boldsymbol{\tau}} = -\mathbb{E}_{\mathbf{z}|\boldsymbol{\theta}} \left[\frac{\partial^2 \ell(\mathbf{z}; \boldsymbol{\theta})}{\partial \mathbf{u} \partial \boldsymbol{\tau}} \right] = \frac{1}{\sigma^2} \mathbf{1} \otimes [\mathbf{u}_x^T, \mathbf{u}_y^T]^T, \quad (80)$$

where \mathbf{I}_{N_p} is the identity matrix of size $N_p \times N_p$ (idem for \mathbf{I}_K), $\mathbf{1}$ is a vector of ones of size K , \otimes is the Kronecker

product, $\mathbf{u}_x, \mathbf{u}_y$ are the derivatives of the latent image \mathbf{u} in the horizontal and vertical directions respectively, and

$$\mathbf{Q} = \begin{bmatrix} \mathbf{u}_x^T \mathbf{u}_x & \mathbf{u}_x^T \mathbf{u}_y \\ \mathbf{u}_x^T \mathbf{u}_y & \mathbf{u}_y^T \mathbf{u}_y \end{bmatrix}. \quad (81)$$

Using the block matrix inversion principle [47], the inverse of \mathbf{J}_D can be expressed as

$$\mathbf{J}_D^{-1} = \begin{bmatrix} \mathbf{S}_u^{-1} & \mathbf{J}_{uu}^{-1} \mathbf{J}_{u\tau} \mathbf{S}_\tau^{-1} \\ \mathbf{S}_\tau^{-1} \mathbf{J}_{u\tau}^T \mathbf{J}_{uu}^{-1} & \mathbf{S}_\tau^{-1} \end{bmatrix}, \quad (82)$$

where

$$\mathbf{S}_u = \mathbf{J}_{uu} - \mathbf{J}_{u\tau} \mathbf{J}_{\tau\tau}^{-1} \mathbf{J}_{u\tau}^T, \quad \mathbf{S}_\tau = \mathbf{J}_{\tau\tau} - \mathbf{J}_{u\tau}^T \mathbf{J}_{uu}^{-1} \mathbf{J}_{u\tau}. \quad (83)$$

From (78)–(80) and (83) we have,

$$\mathbf{S}_\tau^{-1} = \sigma^2 (\mathbf{I}_K + \mathbf{1}\mathbf{1}^T) \otimes \mathbf{Q}^{-1}. \quad (84)$$

The Cramér-Rao bound in (16) follows from (84).

APPENDIX B

BAYESIAN CRAMÉR-RAO BOUND WITH SHIFTS PRIOR

Let \mathbf{z} be $(K+1)$ independent samples following model (2), and assuming that \mathbf{u} is an unknown deterministic image and $\boldsymbol{\tau}$ is a random variable following a generalized Gaussian prior $p(\boldsymbol{\tau})$ given by (22), the joint log-likelihood $\ell(\mathbf{z}, \boldsymbol{\theta})$, with $\boldsymbol{\theta} = [\mathbf{u}^T, \boldsymbol{\tau}^T]^T$ is given by

$$\ell(\mathbf{z}, \boldsymbol{\tau}; \mathbf{u}) = \log p(\mathbf{z}|\boldsymbol{\tau}; \mathbf{u}) + \log p(\boldsymbol{\tau}). \quad (85)$$

Hence, from (21) the Bayesian FIM becomes

$$\mathbf{J}_B = -\mathbb{E}_{\mathbf{z}, \boldsymbol{\tau}|\mathbf{u}} \left[\frac{\partial^2 \log p(\mathbf{z}|\boldsymbol{\tau}; \mathbf{u})}{\partial \boldsymbol{\theta}^2} \right] - \mathbb{E}_{\boldsymbol{\tau}} \left[\frac{\partial^2 \log p(\boldsymbol{\tau})}{\partial \boldsymbol{\theta}^2} \right]. \quad (86)$$

Next, from (77),

$$\begin{aligned} \mathbb{E}_{\mathbf{z}, \boldsymbol{\tau}|\mathbf{u}} \left[\frac{\partial^2 \log p(\mathbf{z}|\boldsymbol{\tau}; \mathbf{u})}{\partial \boldsymbol{\theta}^2} \right] &= \mathbb{E}_{\boldsymbol{\tau}} \left[\mathbb{E}_{\mathbf{z}|\mathbf{u}, \boldsymbol{\tau}} \left[\frac{\partial^2 \log p(\mathbf{z}|\boldsymbol{\tau}; \mathbf{u})}{\partial \boldsymbol{\theta}^2} \right] \right] \\ &= -\mathbb{E}_{\boldsymbol{\tau}} [\mathbf{J}_D] = -\mathbf{J}_D. \end{aligned} \quad (87)$$

For the generalized prior (22), it can be shown that [48]

$$-\mathbb{E}_{\boldsymbol{\tau}} \left[\frac{\partial^2 \log p(\boldsymbol{\tau})}{\partial \boldsymbol{\tau}^2} \right] = \frac{1}{\lambda^2} \mathbf{I}_{2K}, \quad (88)$$

where $\lambda^2 \stackrel{\text{def}}{=} \frac{\delta^2 \Gamma^2(1/c)}{c^2 \Gamma(3/c) \Gamma(2-1/c)}$. Hence, from (86)–(88),

$$\mathbf{J}_B = \mathbf{J}_D + \mathbf{J}_p, \quad \text{with} \quad \mathbf{J}_p = \begin{bmatrix} 0 & 0 \\ 0 & \frac{1}{\lambda^2} \mathbf{I}_{2K} \end{bmatrix}. \quad (89)$$

Using the block matrix inversion principle [42], the inverse of \mathbf{J}_B can be expressed as

$$\mathbf{J}_B^{-1} = \begin{bmatrix} \bar{\mathbf{S}}_u^{-1} & \mathbf{J}_{uu}^{-1} \mathbf{J}_{u\tau} \mathbf{S}_\tau^{-1} \\ \mathbf{S}_\tau^{-1} \mathbf{J}_{u\tau}^T \mathbf{J}_{uu}^{-1} & \mathbf{S}_\tau^{-1} \end{bmatrix}, \quad (90)$$

with

$$\bar{\mathbf{S}}_u = \mathbf{J}_{uu} - \mathbf{J}_{u\tau} (\mathbf{J}_{\tau\tau} + \frac{1}{\lambda^2} \mathbf{I}_{2K})^{-1} \mathbf{J}_{u\tau}^T \quad (91)$$

$$\bar{\mathbf{S}}_\tau = \mathbf{J}_{\tau\tau} + \frac{1}{\lambda^2} \mathbf{I}_{2K} - \mathbf{J}_{u\tau}^T \mathbf{J}_{uu}^{-1} \mathbf{J}_{u\tau}. \quad (92)$$

where $\mathbf{J}_{uu}, \mathbf{J}_{\tau\tau}$ and $\mathbf{J}_{u\tau}$ are given by (78)–(80). Hence,

$$\bar{\mathbf{S}}_\tau = \frac{1}{\sigma^2} (\mathbf{I} - (K+1) \mathbf{1}\mathbf{1}^T) \otimes \mathbf{Q} + \frac{1}{\lambda^2} \mathbf{I}, \quad (93)$$

and

$$\begin{aligned} \bar{\mathbf{S}}_\tau^{-1} &= \mathbf{I} \otimes \left(\frac{1}{\sigma^2} \mathbf{Q} + \frac{1}{\lambda^2} \mathbf{I} \right)^{-1} \\ &+ \mathbf{1}\mathbf{1}^T \otimes \lambda^2 \left((K+2) \mathbf{I} + \frac{\lambda^2}{\sigma^2} \mathbf{Q} + (K+1) \frac{\sigma^2}{\lambda^2} \mathbf{Q}^{-1} \right)^{-1}. \end{aligned} \quad (94)$$

The Bayesian Cramér Rao bound in (28) follows from (94).

APPENDIX C

CRAMÉR-RAO BOUND: STOCHASTIC IMAGE MODEL

Let $\tilde{\mathbf{z}}$ be given by (30). This random variable follows a complex Gaussian distribution with zero mean and covariance matrix $\boldsymbol{\Sigma}$ given by (31). The FIM corresponding to the complex Gaussian process $\tilde{\mathbf{z}}$ is given by [18, Ap. 15C]

$$\{\mathbf{J}_S\}_{i_h, j_q} = \sum_{l=1}^M \text{tr} \left(\boldsymbol{\Sigma}_\tau^{-1}(\boldsymbol{\omega}_l) \frac{\partial \boldsymbol{\Sigma}_\tau(\boldsymbol{\omega}_l)}{\partial \tau_{i_h}} \boldsymbol{\Sigma}_\tau^{-1}(\boldsymbol{\omega}_l) \frac{\partial \boldsymbol{\Sigma}_\tau(\boldsymbol{\omega}_l)}{\partial \tau_{j_q}} \right), \quad (95)$$

where $i, j = 1, \dots, K$, and $h, q \in \{x, y\}$ index the two components of each 2D shift vector $\boldsymbol{\tau}_i$. The spatial frequency $\boldsymbol{\omega}_l, l(l_x, l_y) = 1, \dots, M$ with $M = m_c + \frac{m_r}{2} + 2$ indexes the 2D frequencies $\boldsymbol{\omega}_l = [\omega_{l_x}, \omega_{l_y}]^T$ with $\omega_{l_x} = \frac{2\pi l_x}{m_c}, l_x = -\frac{m_c}{2}, \dots, \frac{m_c}{2}$ and $\omega_{l_y} = \frac{2\pi l_y}{m_r}, l_y = 0, \dots, \frac{m_r}{2}$. To simplify notation, we avoid in the following the subindex l on $\boldsymbol{\omega}$. The matrix $\boldsymbol{\Sigma}_\tau(\boldsymbol{\omega})$ can be decomposed as

$$\boldsymbol{\Sigma}_\tau(\boldsymbol{\omega}) = S(\boldsymbol{\omega}) \mathbf{P}_\tau(\boldsymbol{\omega}) \mathbf{P}_\tau(\boldsymbol{\omega})^H + N(\boldsymbol{\omega}) \mathbf{I}_{K+1}, \quad (96)$$

with

$$\mathbf{P}_\tau(\boldsymbol{\omega}) = [1, e^{i\boldsymbol{\omega} \cdot \boldsymbol{\tau}_1}, e^{i\boldsymbol{\omega} \cdot \boldsymbol{\tau}_2}, \dots, e^{i\boldsymbol{\omega} \cdot \boldsymbol{\tau}_K}]^T. \quad (97)$$

Using the Sherman-Morrison formula [42],

$$\boldsymbol{\Sigma}_\tau^{-1}(\boldsymbol{\omega}) = N^{-1}(\boldsymbol{\omega}) \left(\mathbf{I}_{K+1} + \alpha(\boldsymbol{\omega}) \mathbf{P}_\tau(\boldsymbol{\omega}) \mathbf{P}_\tau(\boldsymbol{\omega})^H \right), \quad (98)$$

where

$$\alpha(\boldsymbol{\omega}) = -\frac{S(\boldsymbol{\omega})}{N(\boldsymbol{\omega}) + (K+1)S(\boldsymbol{\omega})}. \quad (99)$$

To simplify notation we avoid in the following the dependence on $\boldsymbol{\omega}$. Hence we have

$$\boldsymbol{\Sigma}_\tau^{-1} \frac{\partial \boldsymbol{\Sigma}_\tau}{\partial \tau_{i_h}} = N^{-1} \left(\frac{\partial \boldsymbol{\Sigma}_\tau}{\partial \tau_{i_h}} + \alpha \mathbf{P}_\tau \mathbf{P}_\tau^H \frac{\partial \boldsymbol{\Sigma}_\tau}{\partial \tau_{i_h}} \right), \quad (100)$$

and

$$\begin{aligned} \text{tr} \left(\boldsymbol{\Sigma}_\tau^{-1} \frac{\partial \boldsymbol{\Sigma}_\tau}{\partial \tau_{i_h}} \boldsymbol{\Sigma}_\tau^{-1} \frac{\partial \boldsymbol{\Sigma}_\tau}{\partial \tau_{j_q}} \right) &= \\ N^{-1} \left[\text{tr} \left(\frac{\partial \boldsymbol{\Sigma}_\tau}{\partial \tau_{i_h}} \frac{\partial \boldsymbol{\Sigma}_\tau}{\partial \tau_{j_q}} \right) + 2\alpha \text{tr} \left(\frac{\partial \boldsymbol{\Sigma}_\tau}{\partial \tau_{i_h}} \mathbf{P}_\tau \mathbf{P}_\tau^H \frac{\partial \boldsymbol{\Sigma}_\tau}{\partial \tau_{j_q}} \right) \right. \\ &\left. + \alpha^2 \text{tr} \left(\mathbf{P}_\tau \mathbf{P}_\tau^H \frac{\partial \boldsymbol{\Sigma}_\tau}{\partial \tau_{i_h}} \mathbf{P}_\tau \mathbf{P}_\tau^H \frac{\partial \boldsymbol{\Sigma}_\tau}{\partial \tau_{j_q}} \right) \right]. \end{aligned} \quad (101)$$

Substituting (101) in (95) and computing the derivatives,

$$\mathbf{J}_S = [(K+1) \mathbf{I}_K - \mathbf{1}\mathbf{1}^T] \otimes \mathbf{B}, \quad \text{with} \quad \mathbf{B} = \begin{bmatrix} \rho_{x,x} & -\rho_{x,y} \\ -\rho_{x,y} & \rho_{y,y} \end{bmatrix}, \quad (102)$$

$$\rho_{h,q} = \sum_{l=1}^M \frac{2S^2(\boldsymbol{\omega}_l) \omega_{l_h} \omega_{l_q}}{N^2(\boldsymbol{\omega}_l) + (K+1)S(\boldsymbol{\omega}_l)N(\boldsymbol{\omega}_l)}. \quad (103)$$

Hence, we have

$$\mathbf{J}_S^{-1} = \frac{1}{(K+1)} (\mathbf{I}_K + \mathbf{1}\mathbf{1}^T) \otimes \mathbf{B}^{-1}. \quad (104)$$

Then, the error on the shifts estimates is bounded by

$$\text{MSE} \geq \frac{1}{2K} \text{tr}(\mathbf{J}_S^{-1}) = \frac{1}{(K+1)} \left(\frac{\rho_{x,x}^2 + \rho_{y,y}^2}{\rho_{x,x}\rho_{y,y} - \rho_{x,y}^2} \right). \quad (105)$$

Notice that if $S(\boldsymbol{\omega})$ and $N(\boldsymbol{\omega})$ are rotational symmetric (rotation invariant), we have $\rho_{x,y} = 0$ and $\rho_{x,x} = \rho_{y,y}$. In that case, the CRB bound on the MSE (105) becomes

$$\text{CRBS} \stackrel{\text{def}}{=} \frac{2}{(K+1)\rho_{x,x}} = \frac{2}{(K+1)\rho_{y,y}}. \quad (106)$$

High SNR performance. When the signal-to-noise ratio is very high, i.e., $S(\boldsymbol{\omega})/N(\boldsymbol{\omega}) \gg 1$, we have that

$$\rho_{x,x} \xrightarrow{S/N \rightarrow \infty} \rho_{x,x}^{\text{HSNR}} = \sum_{l=1}^M \frac{2S(\boldsymbol{\omega}_l) \omega_x^2}{(K+1)N(\boldsymbol{\omega})}. \quad (107)$$

Let us assume the noise is white with $N(\boldsymbol{\omega}) = \sigma^2$. Since,

$$\sum_{l=1}^M S(\boldsymbol{\omega}_l) \omega_{l_x}^2 \approx \frac{N_p}{(2\pi)^2} \int_0^\pi \int_{-\pi}^\pi S(\boldsymbol{\omega}) \omega_x^2 d\omega_x d\omega_y, \quad (108)$$

$$= \frac{1}{2} \frac{N_p}{(2\pi)^2} \int_{-\pi}^\pi \int_{-\pi}^\pi S(\boldsymbol{\omega}) \omega_x^2 d\omega_x d\omega_y. \quad (109)$$

Then, the CRBS for a rotation invariant process (Eq. (106)) under high SNR simplifies to

$$\text{CRBS}^{\text{HSNR}} \stackrel{\text{def}}{=} \frac{2\sigma^2(2\pi)^2}{N_p \int S(\boldsymbol{\omega}) \omega_x^2 d\boldsymbol{\omega}}. \quad (110)$$

This bound is independent of the number of images K . As we show at follows, it agrees with the deterministic CRB.

Let \mathbf{u} be a deterministic image with $N_p \gg 1$ pixels, that we assume rotation invariant for simplicity. We can approximate the power spectral density by its empirical power spectrum $S_d(\boldsymbol{\omega})$. Then,

$$\frac{1}{N_p} \mathbf{u}_x^T \mathbf{u}_x = \frac{1}{(2\pi)^2} \int S_d(\boldsymbol{\omega}) \omega_x^2 d\boldsymbol{\omega}. \quad (111)$$

For a rotation invariant image \mathbf{u} , we have that

$$\mathbf{u}_x^T \mathbf{u}_y = \frac{1}{(2\pi)^2} \int \tilde{\mathbf{u}}(\omega_x, \omega_y) \omega_x \omega_y d\omega_x d\omega_y = 0.$$

Next, we have that the deterministic CRB in (16), for a rotation invariant signal, can be rewritten as

$$\text{CRBD} = \frac{2\sigma^2}{\mathbf{u}_x^T \mathbf{u}_x} = \frac{2\sigma^2(2\pi)^2}{N_p \int S_d(\boldsymbol{\omega}) \omega_x^2 d\boldsymbol{\omega}}. \quad (112)$$

That is, the stochastic CRB bound in high SNR agrees with the deterministic CRB.

Flat Spectrum signals. Let us consider the particular case of flat spectrum signals, that is,

$$S(\boldsymbol{\omega}) = \begin{cases} S_w & \text{if } \max(|\omega_x|, |\omega_y|) \leq W/2, \\ 0 & \text{otherwise.} \end{cases} \quad (113)$$

We will also assume that the additive noise spectrum is flat in the same frequency band $[-\frac{W}{2}, \frac{W}{2}]^2$ and zero otherwise.

In this case, if we assume $M \gg 1$, we can consider the sum in (103) for ρ_{xx} , as a Riemann approximation, that is,

$$\rho_{xx} \approx \frac{2N_p}{(2\pi)^2} \int_0^{\frac{W}{2}} \int_0^{\frac{W}{2}} \frac{2S^2 \omega_{l_x}^2}{N^2 + (K+1)SN} d\boldsymbol{\omega} \quad (114)$$

$$= \frac{S^2 W^4 N_p}{3\pi^2 2^4 (N^2 + (K+1)SN)}. \quad (115)$$

Thus, rewriting (115) in terms of the SNR as defined in (49), we obtain that the CRB (Eq. (106)) for white images is:

$$\text{CRBS}_w \stackrel{\text{def}}{=} \frac{8\pi^2 (W^2 + 6\text{SNR}_w(K+1))}{N_p(K+1)\text{SNR}_w^2 3W^2}. \quad (116)$$

Natural images. One classical assumption when modeling natural images is that the power spectrum falls quadratically with the Fourier frequency. Let us assume that the considered underlying image follows this law, that is,

$$S(\boldsymbol{\omega}) = \begin{cases} S_n \|\boldsymbol{\omega}\|^{-2} & \text{if } \max(|\omega_x|, |\omega_y|) \leq W/2, \\ 0 & \text{otherwise.} \end{cases} \quad (117)$$

Similarly as for the white signals, let us assume that the additive noise spectrum is flat in the same frequency band $[-\frac{W}{2}, \frac{W}{2}]^2$ taking value N and zero otherwise. We can approximate the sum in ρ_{xx} (Eq. (103)) by,

$$\rho_{xx} \approx \frac{2N_p}{(2\pi)^2} \int_0^{\frac{W}{2}} \int_0^{\frac{W}{2}} \frac{2(\frac{S_n}{N})^2 \omega_x^2}{(\omega_x^2 + \omega_y^2)^2 + \frac{S_n}{N}(K+1)(\omega_x^2 + \omega_y^2)} d\boldsymbol{\omega}. \quad (118)$$

Due to symmetry,

$$\int_0^{\frac{W}{2}} \int_0^{\frac{W}{2}} \frac{2S_n^2 \omega_x^2}{N^2(\omega_x^2 + \omega_y^2)^2 + (K+1)S_n N(\omega_x^2 + \omega_y^2)} d\boldsymbol{\omega} \quad (119)$$

$$= \int_0^{\frac{W}{2}} \int_0^{\frac{W}{2}} \frac{S_n^2(\omega_x^2 + \omega_y^2)}{N^2(\omega_x^2 + \omega_y^2)^2 + (K+1)S_n N(\omega_x^2 + \omega_y^2)} d\boldsymbol{\omega} \quad (120)$$

$$\approx \frac{\pi}{2} \int_0^{\frac{W}{\sqrt{\pi}}} \frac{S_n^2 r}{N^2 r^2 + (K+1)S_n N} dr \quad (121)$$

$$= \frac{\pi}{2} S_n^2 \text{acoth} \left(1 + \frac{2\pi(K+1)S_n}{W^2 N} \right). \quad (122)$$

The approximation in (120) is done by changing the area of integration from $[0, \frac{W}{2}]^2$ to the quarter of circle $[0, \frac{\pi}{2}]$ of radius $\frac{W}{\sqrt{\pi}}$. This is the maximum overlapping circular region that covers the same area as the original one. Thus, under the considered natural image model, the CRB in (106) can be approximated by

$$\text{CRBS}_n \stackrel{\text{def}}{=} \frac{8\pi}{N_p(K+1)\text{SNR}_n^2 \text{acoth} \left(1 + \frac{2\pi(K+1)\text{SNR}_n}{W^2} \right)}, \quad (123)$$

where SNR_n is defined in (44).

APPENDIX D

EXTENDED ZIV-ZAKAI BOUND: PROBABILITY OF ERROR

The computation of the Extended Ziv-Zakai bound requires computing the probability of error $P_{\min}^{\text{el}}(\boldsymbol{\varphi}, \boldsymbol{\varphi} + \boldsymbol{\delta})$, for the

equally likely hypothesis case. This probability can be tightly approximated [41, Eq. (2.243)] by

$$P_{\min}^{\text{el}}(\boldsymbol{\varphi}, \boldsymbol{\varphi} + \boldsymbol{\delta}) \approx \frac{1}{2} \exp \left\{ \mu(s_m) + \frac{s_m^2}{2} \mu''(s_m) \right\} \Phi \left(s_m \sqrt{\mu''(s_m)} \right) + \frac{1}{2} \exp \left\{ \mu(s_m) + \frac{(s_m-1)^2}{2} \mu''(s_m) \right\} \Phi \left((1-s_m) \sqrt{\mu''(s_m)} \right) \quad (124)$$

where

$$\mu(s) = \log \int [p(\tilde{\mathbf{z}} | \boldsymbol{\varphi})]^s [p(\tilde{\mathbf{z}} | \boldsymbol{\varphi} + \boldsymbol{\delta})]^{1-s} d\tilde{\mathbf{z}}, \quad (125)$$

s_m verifies $\mu'(s_m) = 0$ and $\Phi(t) = \frac{1}{\sqrt{2\pi}} \int_t^\infty e^{-\frac{t^2}{2}} dt$.

Assuming that the Fourier coefficients at different frequencies are statistically uncorrelated this becomes

$$\mu(s) = - \sum_{l=1}^M \left\{ s \log |\boldsymbol{\Sigma}_{\boldsymbol{\tau}+\boldsymbol{\delta}}(\boldsymbol{\omega}_l)| + (1-s) \log |\boldsymbol{\Sigma}_{\boldsymbol{\tau}}(\boldsymbol{\omega}_l)| + \log \left(|s \boldsymbol{\Sigma}_{\boldsymbol{\tau}+\boldsymbol{\delta}}^{-1}(\boldsymbol{\omega}_l) + (1-s) \boldsymbol{\Sigma}_{\boldsymbol{\tau}}^{-1}(\boldsymbol{\omega}_l)| \right) \right\}, \quad (126)$$

where $\boldsymbol{\Sigma}_{\boldsymbol{\tau}}(\boldsymbol{\omega})$ is defined in (96). By doing some algebra manipulations one can see that

$$|\boldsymbol{\Sigma}_{\boldsymbol{\tau}}(\boldsymbol{\omega})| = |\boldsymbol{\Sigma}_{\boldsymbol{\tau}+\boldsymbol{\delta}}(\boldsymbol{\omega})| = N(\boldsymbol{\omega})^K (N(\boldsymbol{\omega}) + (K+1)S(\boldsymbol{\omega})). \quad (127)$$

Next, from (98) we can rewrite the determinant in the second term of (126) as,

$$\begin{aligned} & |s \boldsymbol{\Sigma}_{\boldsymbol{\tau}+\boldsymbol{\delta}}^{-1}(\boldsymbol{\omega}_l) + (1-s) \boldsymbol{\Sigma}_{\boldsymbol{\tau}}^{-1}(\boldsymbol{\omega}_l)| \\ &= N(\boldsymbol{\omega})^{-(K+1)} \left(1 + s\alpha(\boldsymbol{\omega})(K+1) \right) \\ & \cdot \left(1 + (1-s)\alpha(\boldsymbol{\omega})((K+1) - \beta(\boldsymbol{\omega})T(\boldsymbol{\delta}, \boldsymbol{\omega})) \right), \end{aligned} \quad (128)$$

where

$$\beta(\boldsymbol{\omega}) = \frac{s\alpha(\boldsymbol{\omega})}{1+(K+1)s\alpha(\boldsymbol{\omega})}, \quad T(\boldsymbol{\delta}, \boldsymbol{\omega}) = \left| 1 + \sum_{j=1}^K e^{-i\boldsymbol{\delta}_j \cdot \boldsymbol{\omega}} \right|^2. \quad (129)$$

Thus substituting (127) and (128) in (126) one obtains,

$$\mu(s) = - \sum_{l=1}^M \log \left[1 + 4s(1-s)\gamma(\boldsymbol{\delta}, \boldsymbol{\omega}_l) \right], \quad (130)$$

where

$$\gamma(\boldsymbol{\delta}, \boldsymbol{\omega}_l) = \frac{S(\boldsymbol{\omega}_l)^2 ((K+1)^2 - T(\boldsymbol{\delta}, \boldsymbol{\omega}_l))}{4N(\boldsymbol{\omega}_l)^2 + (K+1)N(\boldsymbol{\omega}_l)S(\boldsymbol{\omega}_l)}. \quad (131)$$

Thus,

$$\mu'(s) = \sum_{l=1}^M \frac{4\gamma(\boldsymbol{\delta}, \boldsymbol{\omega}_l)(2s-1)}{1+4s(1-s)\gamma(\boldsymbol{\delta}, \boldsymbol{\omega}_l)} \quad (132)$$

and the point such that $\mu'(s_m) = 0$ is $s_m = 1/2$. Then

$$\mu(\tfrac{1}{2}) = - \sum_{l=1}^M \log(1+\gamma(\boldsymbol{\delta}, \boldsymbol{\omega}_l)), \quad \mu''(\tfrac{1}{2}) = \sum_{l=1}^M \frac{8\gamma(\boldsymbol{\delta}, \boldsymbol{\omega}_l)}{1+\gamma(\boldsymbol{\delta}, \boldsymbol{\omega}_l)}. \quad (133)$$

Finally, the probability of error can be approximated by

$$P_{\min}^{\text{el}}(\boldsymbol{\tau}, \boldsymbol{\tau} + \boldsymbol{\delta}) \approx \frac{1}{2} \exp \{ a(\boldsymbol{\delta}) + b(\boldsymbol{\delta}) \} \Phi \left(\sqrt{2b(\boldsymbol{\delta})} \right), \quad (134)$$

where

$$a(\boldsymbol{\delta}) = - \sum_{l=1}^M \log(1+\gamma(\boldsymbol{\delta}, \boldsymbol{\omega}_l)), \quad b(\boldsymbol{\delta}) = \sum_{l=1}^M \frac{\gamma(\boldsymbol{\delta}, \boldsymbol{\omega}_l)}{1+\gamma(\boldsymbol{\delta}, \boldsymbol{\omega}_l)}, \quad (135)$$

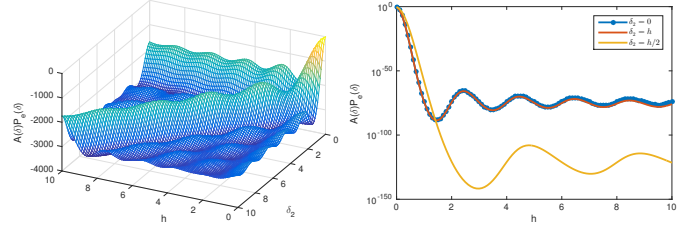


Figure A.1: Visualization of an example function $g(h, \delta_2)$ given by (141) (left), and different cuts of $g(h, \delta_2)$ at $\delta_2 = 0, h, h/2$ (right). For low h values, the maximum of g happens at $(h, h/2)$, while for large values it happens at $(h, 0)$.

APPENDIX E

EXTENDED ZIV-ZAKAI BOUND FOR WHITE SIGNALS

To simplify the analysis we consider one-dimensional random signals with a constant power spectral density $S(\omega)$ in $[-\frac{W}{2}, \frac{W}{2}]$ and zero otherwise, and zero-mean Gaussian noise with flat spectrum $N(\omega) = N$ in the same frequency band. We closely follow the deduction in [29].

First, assuming $N_p \gg 1$, let us approximate $a(\boldsymbol{\delta})$ and $b(\boldsymbol{\delta})$ in (135) for the particular case of white signals,

$$a(\boldsymbol{\delta}) = -\frac{N_p}{2\pi} \int_0^{W/2} \log \left[1 + \gamma(\boldsymbol{\delta}, \omega) \right] d\omega, \quad (136)$$

$$b(\boldsymbol{\delta}) = \frac{N_p}{2\pi} \int_0^{W/2} \frac{\gamma(\boldsymbol{\delta}, \omega)}{1 + \gamma(\boldsymbol{\delta}, \omega)} d\omega, \quad (137)$$

and

$$\gamma(\boldsymbol{\delta}, \omega) = \frac{S^2((K+1)^2 - T(\boldsymbol{\delta}, \omega))}{4(N^2 + (K+1)NS)}. \quad (138)$$

To evaluate the Extended Ziv-Zakai bound in estimating one single component of $\boldsymbol{\tau} = [\tau_1, \tau_2, \dots, \tau_M]$, we can choose without loss of generality $\mathbf{a} = [1, 0, \dots, 0]$ in (56). Thus, evaluation of the EZZB requires computing

$$\epsilon_1^2 \geq \int_0^\infty P_A(h) dh, \quad (139)$$

where we have defined

$$P_A(h) = \mathcal{V} \left\{ \max_{\boldsymbol{\delta}: \delta_1=h} A(\boldsymbol{\delta}) P_{\min}^{\text{el}}(\boldsymbol{\delta}) \right\}. \quad (140)$$

Note that to solve (139) one needs to maximize

$$g(\boldsymbol{\delta}) = A(\boldsymbol{\delta}) P_{\min}^{\text{el}}(\boldsymbol{\delta}) \quad (141)$$

with respect to $[\delta_2, \dots, \delta_K]$ for each value of $\delta_1 = h$. A lossy (in general) lower bound can be obtained by setting the unspecified components of $\boldsymbol{\delta}$ to zero. Due to the symmetry of the problem it is clear that the maximum should be attained at $\boldsymbol{\delta}$ such that $\delta_2 = \delta_3 = \dots = \delta_K$. Thus, to simplify the exposition, let us do an abuse of notation and refer to $\boldsymbol{\delta}$ as the couple $[\delta_1, \delta_2]$, and omit $\delta_3, \dots, \delta_K$ assuming that they are all equal to δ_2 .

An example of the function $g(\delta_1, \delta_2)$ is shown in Figure A.1. From Figure A.1 it is clear that there are roughly two different behaviors of g : one in the vicinity of $h \approx 0$ where the maximum of $g(h, \delta_2)$ is obtained at $\delta_2 = h/2$, while when $h \gg 0$ the maximum is obtained at $\delta_2 = 0$. In what follows,

we approximate the probability of error in these two different scenarios in order to reach a simplified version of the EZZB.

Small values of h . Let us note that

$$a(\delta) + b(\delta) \geq -\frac{1}{2} \frac{N_p}{2\pi} \int_0^{W/2} \gamma(\omega, \delta)^2 d\omega, \quad (142)$$

which is a direct consequence of $\log(1+x) - \frac{x}{1+x} \leq \frac{x^2}{2}$, for $x \geq 0$. Also, since $x/(1+x) \leq x$, for $x \geq 0$, we have,

$$c(\delta) \stackrel{\text{def}}{=} 2b(\delta) \leq \frac{N_p}{\pi} \int_0^{W/2} \gamma(\omega, \delta) d\omega. \quad (143)$$

Thus, for the particular case $\delta = [h, h/2]$, we have

$$(K+1)^2 - T(h, \frac{h}{2}) = 8(K-1) \sin^2(\frac{\omega h}{4}) + 4 \sin^2(\frac{\omega h}{2}) \quad (144)$$

$$\leq \frac{(K+1)}{2} h^2 \omega^2. \quad (145)$$

The last inequality is due the fact that $\sin^2(x) \leq x^2$. This leads to an upper bound on γ , Equation (138),

$$\gamma(h, \frac{h}{2}, \omega) \geq \frac{\kappa_1 \omega^2 h^2}{4}, \quad \text{with} \quad \kappa_1 = \frac{S^2(K+1)}{2N^2+2(K+1)NS}. \quad (146)$$

Thus, the probability of error can be approximately lower bounded by

$$P_{\min}^{\text{el}}(h, \frac{h}{2}) \approx e^{a(h, \frac{h}{2})+b(h, \frac{h}{2})} \Phi(c(h, \frac{h}{2})) \geq e^{-d^4 h^4} \Phi(ch) \quad (147)$$

where

$$d^4 = \frac{W^5 N_p \kappa_1^2}{\pi \cdot 5 \cdot 2^{11}} \quad \text{and} \quad c^2 = \frac{W^3 N_p \kappa_1}{\pi \cdot 3 \cdot 2^5}.$$

Note that this lower bound on the probability of error is valid for the whole domain of h and thus can be used to obtain a lower bound on the performance of any estimator of τ . For the case $\delta = [h, \frac{h}{2}]$ the function $A(\delta)$ given by (58) takes the form,

$$A(h, \frac{h}{2}) = (1 - \frac{h}{D})(1 - \frac{h}{2D})^{K-1}. \quad (148)$$

Next, we have the following lower bound

$$P_A(h) \geq A(h, \frac{h}{2}) P_{\min}^{\text{el}}(h, \frac{h}{2}) \geq f_1(h), \quad (149)$$

where

$$f_1(h) = (1 - \frac{h}{D})(1 - \frac{h}{2D})^{K-1} e^{-d^4 h^4} \Phi(ch). \quad (150)$$

When K is very large, the factor $(1 - \frac{h}{2D})^{K-1}$ in $A(h, \frac{h}{2})$ significantly attenuates the probability of error. In this particular case, $\delta = [h, 0]$ may lead to a tighter lower bound. Nevertheless, we will not consider this scenario.

Large values of h . For large values of h , we will bound the performance with its value at $\delta = [h, 0]$. According to Figure A.1, this is the tightest path to maximize g in the region $h \gg 0$. In this case, the function

$$g(h, 0) = (1 - h/D) P_{\min}^{\text{el}}(h, 0), \quad (151)$$

oscillates outside the vicinity of 0 as illustrated in Figure A.1. If h_0, h_1, \dots, h_L are the local maxima of $P_{\min}^{\text{el}}(h, 0)$, then the function $\mathcal{V}\{g(h, 0)\}$, is tightly lower bounded by

$$\mathcal{V}\{g(h, 0)\} \leq (1 - \frac{h_j}{D}) P_{\min}^{\text{el}}(h_j, 0) \quad \text{for} \quad h_{j-1} \leq h \leq h_j. \quad (152)$$

Moreover, since the function $\mathcal{V}\{g(h, 0)\}$ is non-increasing (by definition), this is true for any given set of $\{h_n\}$. For simplicity, let us chose $h_j = \frac{2\pi}{W} j$, for $j = 0, 1, \dots$

Thus, doing similar algebraic operations as before but at $\delta = [h, 0]$ we obtain

$$(K+1)^2 - T(h, 0) = 4K \sin^2(\omega h/2) \quad (153)$$

and substituting (153) in (138), we obtain

$$\gamma(h, 0, \omega) = \kappa_2 \sin^2(\omega h/2), \quad \text{with} \quad \kappa_2 = \frac{S^2 K}{N^2 + (K+1)NS}. \quad (154)$$

In this case, the probability of error $P_{\min}^{\text{el}}(h_j, 0)$ can be tightly approximated by (134),

$$P_{\min}^{\text{el}}(h_j, 0) \approx e^{a(h_j, 0)+b(h_j, 0)} \Phi(c(h_j, 0)), \quad (155)$$

where $a(h_j, 0)$ and $b(h_j, 0)$ are obtained by evaluating (136), (137) and (154) at $h = h_j$, respectively, obtaining

$$a(h_j, 0) = -\frac{W N_p}{2\pi} \log\left(\frac{\sqrt{\kappa_2+1}+1}{2}\right) \stackrel{\text{def}}{=} a, \quad (156)$$

and similarly

$$b(h_j, 0) = \frac{W N_p}{4\pi} \frac{\sqrt{\kappa_2+1}-1}{\sqrt{\kappa_2+1}} \stackrel{\text{def}}{=} b. \quad (157)$$

Note that both equations become independent of j . Next it follows that $P_{\min}^{\text{el}}(h_j, 0) \approx e^{a+b} \Phi(\sqrt{2b})$. Thus,

$$\mathcal{V}\{g(h, 0)\} \geq (1 - \frac{h_j}{D}) e^{a+b} \Phi(\sqrt{2b}) \quad \text{for} \quad h_j - \frac{2\pi}{W} \leq h \leq h_j. \quad (158)$$

Since $1 - \frac{h_j}{D} \geq 1 - \frac{2\pi}{DW}$ for $h_j - \frac{2\pi}{W} \leq h \leq h_j$, it follows that

$$P_A(h) \geq \mathcal{V}\{g(h, 0)\} \geq f_2(h), \quad (159)$$

where

$$f_2(h) = \max(1 - \frac{2\pi}{DW} - \frac{h}{D}, 0) e^{a+b} \Phi(\sqrt{2b}). \quad (160)$$

Final Bound. To get the final bound we merge the two previous lower-bounds, (149) and (159), into a single lower bound,

$$P_A(h) \geq \max(f_1(h), f_2(h)). \quad (161)$$

To further simplify the lower bound we can split the domain of integration of h , that is $[0, D]$, and make each one valid in a region. Let $h^* = \sqrt{2b}/c$. This point is close to the intersection of $f_1(h)$ and $f_2(h)$. Thus,

$$P_A(h) \geq \begin{cases} f_1(h) & \text{if } 0 \leq h < h^*, \\ f_2(h) & \text{if } h^* \leq h. \end{cases} \quad (162)$$

Substituting (162) in (139) one obtains a lower bound on the mean square error,

$$\epsilon_1^2 \geq \int_0^{h^*} h f_1(h) dh + \int_{h^*}^D h f_2(h) dh. \quad (163)$$

The first term in (163) can be lower bounded by

$$\int_0^{h^*} h f_1(h) dh \geq (1 - \frac{h^*}{D})(1 - \frac{h^*}{2D})^{K-1} \int_0^{h^*} h e^{-d^4 h^4} \Phi(ch) dh. \quad (164)$$

When K is not very large, $(1 - \frac{h^*}{D})(1 - \frac{h^*}{2D})^{K-1} \approx 1$. Then,

$$\int_0^{h^*} h e^{-d^4 h^4} \Phi(ch) dh = \frac{1}{c^2} \int_0^{\sqrt{2b}} h e^{-\frac{9\pi h^4}{10W N_p}} \Phi(h) dh. \quad (165)$$

The second term in (163) can be (approx.) lower bounded by

$$\begin{aligned} \int_{h^*}^D h f_2(h) dh &= \int_{h^*}^D \max(1 - \frac{2\pi}{WD} - \frac{h}{D}, 0) e^{a+b} \phi(\sqrt{2b}) h dh \\ &\geq e^{a+b} \phi(\sqrt{2b}) \int_{4\sqrt{3}/W}^{D-2\pi/W} \max(1 - \frac{2\pi}{WD} - \frac{h}{D}, 0) h dh \\ &\approx \frac{D^2}{6} e^{a+b} \phi(\sqrt{2b}). \end{aligned} \quad (166)$$

From (163), (165) and (166), we get the EZZB bound in (63).

REFERENCES

- [1] P. E. Debevec and J. Malik, "Recovering high dynamic range radiance maps from photographs," in *Proc. An. Conf. Comp. Grap. Inter. Tech. (SIGGRAPH)*, 1997, pp. 369–378.
- [2] C. Aguerrebere, J. Delon, Y. Gousseau, and P. Musé, "Simultaneous HDR image reconstruction and denoising for dynamic scenes," in *Proc. IEEE Int. Conf. Comput. Photogr. (ICCP)*, 2013, pp. 1–11.
- [3] D. Robinson and P. Milanfar, "Statistical performance analysis of super-resolution," *IEEE Trans. Image Process.*, vol. 15, no. 6, pp. 1413–1428, 2006.
- [4] D. Robinson, S. Farsiu, and P. Milanfar, "Optimal registration of aliased images using variable projection with applications to super-resolution," *Comput. J.*, vol. 52, no. 1, pp. 31–42, 2009.
- [5] C. Liu and D. Sun, "On Bayesian adaptive video super resolution," *IEEE Trans. Pattern Anal. Mach. Intell.*, vol. 36, no. 2, pp. 346–360, 2014.
- [6] T. Buades, Y. Lou, J.-M. Morel, and Z. Tang, "A note on multi-image denoising," in *In Proc. of Local and Non-Local Approx. in Image Proc. (LNLA)*, 2009.
- [7] H. Zhang, D. Wipf, and Y. Zhang, "Multi-image blind deblurring using a coupled adaptive sparse prior," in *Proc. IEEE Conf. Comput. Vis. Pattern Recog. (CVPR)*, 2013, pp. 1051–1058.
- [8] M. Delbracio and G. Sapiro, "Burst Deblurring: Removing camera shake through Fourier burst accumulation," in *Proc. IEEE Conf. Comput. Vis. Pattern Recog. (CVPR)*, 2015, pp. 2385–2393.
- [9] R. C. Hardie, K. J. Barnard, and E. E. Armstrong, "Joint map registration and high-resolution image estimation using a sequence of undersampled images," *IEEE Trans. Image Process.*, vol. 6, no. 12, pp. 1621–1633, 1997.
- [10] H. S. Sawhney, S. Hsu, and R. Kumar, "Robust video mosaicing through topology inference and local to global alignment," in *Proc. Europ. Conf. Comput. Vis. (ECCV)*, 1998, pp. 103–119.
- [11] V. M. Govindu, "Lie-algebraic averaging for globally consistent motion estimation," in *Proc. IEEE Conf. Comput. Vis. Pattern Recog. (CVPR)*, 2004, pp. 684–691.
- [12] S. Farsiu, M. Elad, and P. Milanfar, "Constrained, globally optimal, multi-frame motion estimation," in *Proc. Workshop Stat. Signal Process.*, IEEE, 2005, pp. 1396–1401.
- [13] N. A. Woods, N. P. Galatsanos, and A. K. Katsaggelos, "Stochastic methods for joint registration, restoration, and interpolation of multiple undersampled images," *IEEE Trans. Image Process.*, vol. 15, no. 1, pp. 201–213, 2006.
- [14] X. Li, P. Mooney, S. Zheng, C. R. Booth, M. B. Braunfeld, S. Gubbens, D. A. Agard, and Y. Cheng, "Electron counting and beam-induced motion correction enable near-atomic-resolution single-particle cryo-EM," *Nat. Methods*, vol. 10, no. 6, pp. 584–590, 2013.
- [15] A. Bartesaghi, D. Matthies, S. Banerjee, A. Merk, and S. Subramaniam, "Structure of β -galactosidase at 3.2-Å resolution obtained by cryo-electron microscopy," *Proc. Natl. Acad. Sci. U.S.A.*, vol. 111, no. 32, pp. 11 709–11 714, 2014.
- [16] T. Grant and N. Grigorieff, "Measuring the optimal exposure for single particle cryo-em using a 2.6Å reconstruction of rotavirus VP6," *eLife*, 2015.
- [17] J. L. Rubinstein and M. A. Brubaker, "Alignment of cryo-EM movies of individual particles by optimization of image translations," *J. Struct. Biol.*, vol. 192, no. 2, pp. 188–195, 2015.
- [18] S. M. Kay, *Fundamentals of statistical signal processing. [Volume I], Estimation theory*. Prentice Hall, 1993.
- [19] D. Robinson and P. Milanfar, "Fundamental performance limits in image registration," *IEEE Trans. Image Process.*, vol. 13, no. 9, pp. 1185–1199, 2004.
- [20] T. Q. Pham, M. Bezuijen, L. J. van Vliet, K. Schutte, and C. L. Luengo Hendriks, "Performance of optimal registration estimators," in *Proc. SPIE Vis. Inf. Proces.*, vol. 5817, 2005, pp. 133–144.
- [21] C. Aguerrebere, J. Delon, Y. Gousseau, and P. Musé, "Best algorithms for HDR image generation. a study of performance bounds," *SIAM J. Imag. Sci.*, vol. 7, no. 1, pp. 1–34, 2014.
- [22] P. Chatterjee and P. Milanfar, "Is denoising dead?" *IEEE Trans. Image Process.*, vol. 19, no. 4, pp. 895–911, 2010.
- [23] J. Ziv and M. Zakai, "Some lower bounds on signal parameter estimation," *IEEE Trans. Inf. Theory*, vol. 15, no. 3, pp. 386–391, 1969.
- [24] L. P. Seidman, "Performance limitations and error calculations for parameter estimation," *Proc. IEEE*, vol. 58, no. 5, pp. 644–652, 1970.
- [25] D. Chazan, M. Zakai, and J. Ziv, "Improved lower bounds on signal parameter estimation," *IEEE Trans. Inf. Theory*, vol. 21, no. 1, pp. 90–93, 1975.
- [26] K. Bell, Y. Steinberg, Y. Ephraim, and H. Van Trees, "Extended Ziv-Zakai lower bound for vector parameter estimation," *IEEE Trans. Inf. Theory*, vol. 43, no. 2, pp. 624–637, 1997.
- [27] M. Xu, H. Chen, and P. Varshney, "Ziv-Zakai bounds on image registration," *IEEE Trans. Signal Process.*, vol. 57, no. 5, pp. 1745–1755, 2009.
- [28] A. J. Weiss and E. Weinstein, "Fundamental limitations in passive time delay estimation—part I: Narrow-band systems," *IEEE Trans. Acoust., Speech, Signal Process.*, vol. 31, no. 2, pp. 472–486, 1983.
- [29] E. Weinstein and A. J. Weiss, "Fundamental limitations in passive time-delay estimation—part II: Wide-band systems," *IEEE Trans. Acoust., Speech, Signal Process.*, vol. 32, no. 5, pp. 1064–1078, 1984.
- [30] M. Rais, C. Thiebaut, J.-M. Delvit, and J.-M. Morel, "A tight multiframe registration problem with application to earth observation satellite design," in *Proc. IEEE Int. Conf. Imag. Sys. and Tech. (IST)*, Oct 2014, pp. 6–10.
- [31] A. Bhattacharyya, "On some analogues of the amount of information and their use in statistical estimation," *Sankhyā: Indian J. Stat.*, pp. 1–14, 1946.
- [32] E. Barankin, "Locally best unbiased estimates," *Ann. Math. Stat.*, pp. 477–501, 1949.
- [33] J. S. Abel, "A bound on mean-square-estimate error," *IEEE Trans. Inf. Theory*, vol. 39, no. 5, pp. 1675–1680, 1993.
- [34] H. Trees, *Detection, estimation and modulation theory, vol. 1*. Wiley New York, 1968.
- [35] A. J. Weiss, *Fundamental bounds in parameter estimation*. Tel-Aviv University, 1985.
- [36] S. Roth and M. J. Black, "Fields of experts: A framework for learning image priors," in *Proc. IEEE Conf. Comput. Vis. Pattern Recog. (CVPR)*, vol. 2, 2005, pp. 860–867.
- [37] M. Elad and Y. Hel-Or, "A fast super-resolution reconstruction algorithm for pure translational motion and common space-invariant blur," *IEEE Trans. Image Process.*, vol. 10, no. 8, pp. 1187–1193, 2001.
- [38] R. Fransens, C. Strecha, and L. Van Gool, "Optical flow based super-resolution: A probabilistic approach," *Comput. Vis. Image Und.*, vol. 106, no. 1, pp. 106–115, 2007.
- [39] A. Levin, Y. Weiss, F. Durand, and W. T. Freeman, "Understanding and evaluating blind deconvolution algorithms," in *Proc. IEEE Conf. Comput. Vis. Pattern Recog. (CVPR)*, 2009, pp. 1964–1971.
- [40] N. Efrat, D. Glasner, A. Apartsin, B. Nadler, and A. Levin, "Accurate blur models vs. image priors in single image super-resolution," in *Proc. IEEE Int. Conf. Comput. Vis. (ICCV)*, 2013, pp. 2832–2839.
- [41] H. L. Van Trees, K. L. Bell, and Z. Tian, *Detection Estimation and Modulation Theory*. John Wiley & Sons, 2013.
- [42] K. B. Petersen and M. S. Pedersen, "The matrix cookbook," *Technical University of Denmark*, 2012.
- [43] A. Nehorai and M. Hawkes, "Performance bounds for estimating vector systems," *IEEE Trans. Signal Process.*, vol. 48, no. 6, pp. 1737–1749, 2000.
- [44] D. J. Field, "Relations between the statistics of natural images and the response properties of cortical cells," *J. Opt. Soc. Am. A*, vol. 4, no. 12, pp. 2379–2394, 1987.
- [45] Y. Noam and H. Messer, "Notes on the tightness of the hybrid Cramér-Rao lower bound," *IEEE Trans. Signal Process.*, vol. 57, no. 6, pp. 2074–2084, 2009.
- [46] M. Guizar-Sicairos, S. T. Thurman, and J. R. Fienup, "Efficient subpixel image registration algorithms," *Opt. Lett.*, vol. 33, no. 2, pp. 156–158, 2008.
- [47] F. Graybill, *Matrices with Applications in Statistics*, ser. Duxbury Classic Series. Cengage Learning, 2001.
- [48] H. Nguyen and H. L. Van Trees, "Comparison of performance bounds for DOA estimation," in *IEEE Seventh SP Work. on Stat. Sig Array Proc.*, 1994, pp. 313–316.